HYBRID OPTICAL SYSTEMS: FROM NANOMETER TO MULTI-METER SCALES

by

Alexander Ashton Miles

A Dissertation Submitted to the Faculty of the

DEPARTMENT OF OPTICAL SCIENCES

In Partial Fulfillment of the Requirements
For the Degree of

DOCTOR OF PHILOSOPHY

In the Graduate College

THE UNIVERSITY OF ARIZONA

2015

THE UNIVERSITY OF ARIZONA
GRADUATE COLLEGE

As members of the Dissertation Committee, we certify that we have read the dissertation prepared by Alexander Ashton Miles entitled Hybrid Optical Systems: From Nanometer to Multi-meter Scales and recommend that it be accepted as fulfilling the dissertation requirement for the Degree of Doctor of Philosophy.

Date: 19 November 2015
Dr. Robert Norwood

Date: 19 November 2015
Dr. Ewan Wright

Date: 19 November 2015
Dr. Angus Macleod

Final approval and acceptance of this dissertation is contingent upon the candidate's submission of the final copies of the dissertation to the Graduate College.
I hereby certify that I have read this dissertation prepared under my direction and recommend that it be accepted as fulfilling the dissertation requirement.

Date: 19 November 2015
Dissertation Director: Dr. Robert Norwood

STATEMENT BY AUTHOR

This dissertation has been submitted in partial fulfillment of the requirements for an advanced degree at the University of Arizona and is deposited in the University Library to be made available to borrowers under rules of the Library.

Brief quotations from this dissertation are allowable without special permission, provided that an accurate acknowledgement of the source is made. Requests for permission for extended quotation from or reproduction of this manuscript in whole or in part may be granted by the head of the major department or the Dean of the Graduate College when in his or her judgment the proposed use of the material is in the interests of scholarship. In all other instances, however, permission must be obtained from the author.

SIGNED: Alexander Ashton Miles

ACKNOWLEDGEMENTS

I would not have been able to do the work I did, or find any success in these endeavors, without the help of others. I want to thank Prof. Robert Norwood for the support, advocacy, and mentoring he gave me over the last five years. Involved and informed when he needed to be, and always with his student's interest in mind, I could not have asked for a better advisor. I want to thank Prof. Ewan Wright and Prof. Angus Macleod, not only for serving on my committee, but also for providing excellent courses which instilled new interests in me. Dr. Palash Gangopadhyay and Dr. Pierre-Alexandre Blanche were enormously helpful along the way, and taught me a great deal about the practicalities of science. I would also like to thank my research colleagues, Shabnam Virji-Khalfan, Brittany Lynn, Brian Wheelwright, Ben Cromey, Colton Bigler, Byron Cocilovo, Greg Cohoon, and Liliana Ruiz Diaz, for the countless contributions they made to our shared projects. Lastly I'd like to thank Prof. Brian P. Anderson, Ouliana Panova, Kristin Waller, David Melchior, William Duncan, and Joseph Lowney for providing an endless supply of conversation and conviviality over the years.

DEDICATION

To everyone who helped me along the way,
and all those who came before.

TABLE OF CONTENTS

TABLE OF CONTENTS – *Continued*

LIST OF FIGURES

LIST OF TABLES

LIST OF SYMBOLS

Due to the variety of projects addressed in this work, the symbols used will be described below on a per-chapter basis.

Chapter 2		**Chapter 3**	
I	Scattered intensity	B	Magnetic field magnitude or flux density
I_0	Incident intensity	L	Interaction length (i.e. film thickness)
θ	Scattering angle	V	Verdet constant
R	Particle distance	θ	Faraday rotation amount
n	Refractive index of the particles	M	Magnetization
λ	Wavelength of scattered light	χ_m	Magnetic susceptibility
d	Particle diameter	H	Magnetic field
Chapter 4		**Chapter 5**	
C_t	Transverse offset loss	$\overline{R_T}$	Out-of-band reflection
C_θ	Angular offset loss	$\overline{R_R}$	In-band reflection
a	Fiber core diameter	Δ	Cell junction mismatch
σ	Full beam diameter	c_1	Transmission weight
σ_0	Initial beam diameter	c_2	Reflection weight
f	Focal length	c_3	Cell mismatch weight
n_0	Background refractive index	θ	Angle of incidence on mirror
d	Lateral fiber-core offset	θ_{skew}	Residual solar skew angle
z_R	Rayleigh range of the beam	$W(\theta)$	Weighting function
λ	Wavelength of the guided light	m	Merit at a single angle
		M	Overall system merit

CHAPTER 1

Introduction

Completely new ideas are often lauded as the pinnacle of invention; something never before seen that attains new heights of performance. Aside from being an incredibly difficult undertaking, this is not how development generally progresses. Existing solutions to any given problem will invariably possess trade offs. Precious few tools obtain performance without the price, reliability without sacrificing speed, nor precision without sacrificing dynamic range. Combining multiple technologies or materials to improve over-all performance has shown itself to be a good alternative to blind invention. Combining elements in this manner results in what can be referred to as a hybrid.

The projects described in this work concern a number of these hybrids. The collection of projects are limited to optical applications, but are otherwise enormously different. There is perhaps no better way to illustrate this breadth than their characteristic length-scale. That is, the general size of the elements being hybridized. Ten orders of magnitude lie between the smallest system described (composite materials incorporating nanoparticles) and the largest (a utility-scale hybrid solar collector). While I will describe the general thrust of the projects here, each chapter will contain a more detailed background.

Let us start with the smallest element I'll be addressing; a single component of a composite optical material. Given the unique refractive and dispersive properties of diamond, it is an attractive optical material. Unfortunately, the lowest cost diamond available possesses large amounts of impurities and color. In an attempt to remove the visible color from commercially available detonation-origin nanodiamond powders we developed a facile three-step cleaning process. The process involves

isothermal heating, acid treatments, and finally density gradient centrifugation. The resulting nanodiamonds are ultra-pure, containing no detectable non-diamond carbon nor inorganic impurities.

Next we will address a complete composite material system, a combination of a block co-polymer with known self-assembly behaviors with strongly ferromagnetic nanoparticles. This work was performed in collaboration with the Polymer Science Group of Professor James Watkins of the University of Massachusetts Amherst. The applications in mind are magnetic field sensors, used in medical testing and physical experiments, and fiber optic isolators, used extensively in telecommunications networks. Polystyrene-b-poly (2-vinyl pyridine) (PS-b-P2VP) and controlled size iron platinum (FePt) nanoparticles were the materials chosen. Composites made from them exhibited commercially significant Verdet constants in room temperature Faraday rotation measurements, and posses processing benefits over the current state-of-the-art magneto-optically active materials. We have investigated the magneto-optic property of this hybrid material system in terms of particle loading, composite micro-structure, wavelength and temperature. FePt NPs with average core diameters of 2, 4.8, 5.4 and 10 nm were modified with gallic acid and selectively incorporated into the P2VP domain at weight percents from 0.1 % to 25 %. Verdet constants of annealed nanocomposites were measured at four infrared wavelengths (845, 980, 1310 and 1550 nm). The combination of self-assembly of block co-polymer and magnetically responsive nanoparticles provides improved performance over existing non-crystaline materials.

On the scale of the aforementioned fiber optic components, and pulling in the idea of structured refractive index, we implemented and tested a free-space diffraction-based switch with seven single-mode fiber input and output channels. The switch is a hybrid of the micron-scale optics of single-mode fiber modes, and the centimeter scale of free-space holography. Why holography? The driving concern was switching speed, that is, how much time elapses while the switch changes

between configurations, but other methods for switching light are comparable in speed. The real driver is the combination of speed and flexibility, as a hologram enables adding, dropping, mixing, and splitting signals, all in the optical domain, and supporting a scalable number of ports. Built primarily using off-the-shelf components and a commercially available digital micro-mirror device (DMD), the switch is protocol and bit-rate agnostic, robust against random mirror failure, and provides the basic building block for a fully reconfigurable optical add drop multiplexer (ROADM). In addition, the switch is capable of reconfiguring 100 times faster than currently available technologies with comparable port counts. Our design offers the potential to address the growing need for high speed scalable circuit switching for data centers and optical networks.

Pushing the scale further, we address a system that hybridizes two established methods for harvesting solar energy. Sunlight can be captured as electricity using photovoltaics (PV), the most common method on the consumer level, as well as heat (often called concentrated solar power, CSP), which is more common on the utility level. Each approach has benefits. PV cells can be highly efficient over a specific band of wavelengths, but lose efficiency outside that band, meanwhile CSP can utilize almost any wavelength provided, but at a lower efficiency. An additional driving issue is storage. Heat storage is comparatively low cost and effective, while battery technology, needed to store the excess generation from PV cells, remains expensive and difficult to scale. It's clear that a system possessing the peak efficiency of PV, with the deployable storage of CSP, would most effectively meet demand around the clock. In order to combine these approaches, the solar spectrum must be split up into the band best suited to PV, and the remainder to be converted to heat. To that end, we have developed an approach for designing a dichroic coating to optimize performance of such a system utilizing multi-junction photovoltaic cells while diverting unused light to heat collection. By matching the spectral responses of the photovoltaic cells and current matching them, substantial improvement to system efficiencies are shown to be possible. A design for use in a

concentrating hybrid solar collector was produced by this approach.

CHAPTER 2

Purification and Isolation of Nanodiamonds

2.1 Background

Materials provide interesting opportunities for hybridization in the form of composite materials. In essence, a composite is simply the result of combining several materials with distinct physical or chemical properties to produce something more useful. This approach has a rich history, and encompasses more than might be apparent. The earliest composite recorded, and still used in some rural areas, is a lattice work of wood strips reinforced with clay and mud known as wattle and duab; sort of a proto-drywall first used about 6000 years ago[56]. Similarly, concrete is cement reinforced with gravel or sand aggregate, and was first recorded in 25 BC by the Roman engineer Vitruvius[62]. The very same approach has yielded common modern materials, such as carbon-fiber, fiberglass, asphalt, and dental composite. Many of the more recently developed composite materials are purpose-built for aerospace applications and structural materials, but applications in optics are more rare. While there are many optical polymers and epoxies, a filler material that provides unique properties is key.

Diamond possesses a compelling combination of optical properties, namely a very large refractive index without the large chromatic dispersion that it typically entails. When choosing glasses for an optical design, an index-dispersion chart or "glass map" is a common tool. Such a chart with diamond added is provided in Figure 2.1, making clear just how unusual the properties of diamond are. At present, optical grade diamond is typically deposited by chemical vapor deposition and, while capable of producing inch-scale optics, cost and volume continue to be limitations[57]. If diamond could be hybridized with a moldable or castable

host material it would open up an entirely new design space of lower-cost higher-performance optics.

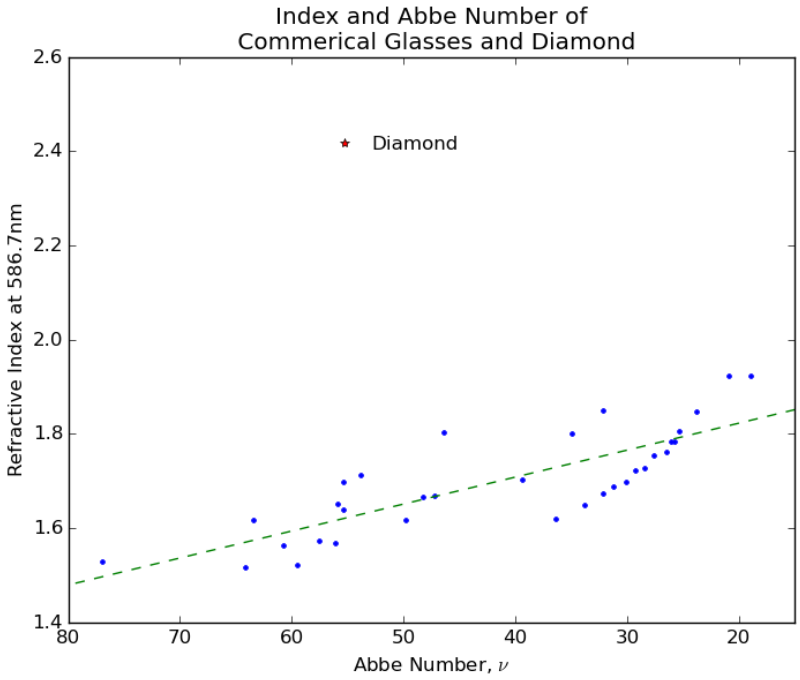

Figure 2.1: Index and dispersion of diamond provide a unique combination when compared with commercially available glasses.

The dielectric constant, and therefore refractive index, of an optical composite can be predicted using the Maxwell-Garnett effective medium approximation[39]. As shown in 2.1, the effective dielectric constant ϵ_{eff} can be determined given ϵ_m the dielectric constant of the matrix, ϵ_f the dielectric constant of the filler, and δ the volume fraction of filler in the matrix. This relation departs slightly from a simple linear variation, as illustrated in Figure 2.2.

$$\epsilon_{eff} = \epsilon_m \frac{2\delta_f (\epsilon_f - \epsilon_m) + \epsilon_f + 2\epsilon_m}{2\epsilon_m + \epsilon_f + \delta_f (\epsilon_m - \epsilon_f)} \tag{2.1}$$

$$n_{eff} = \sqrt{\mathrm{Re}\,(\epsilon_{eff})} \tag{2.2}$$

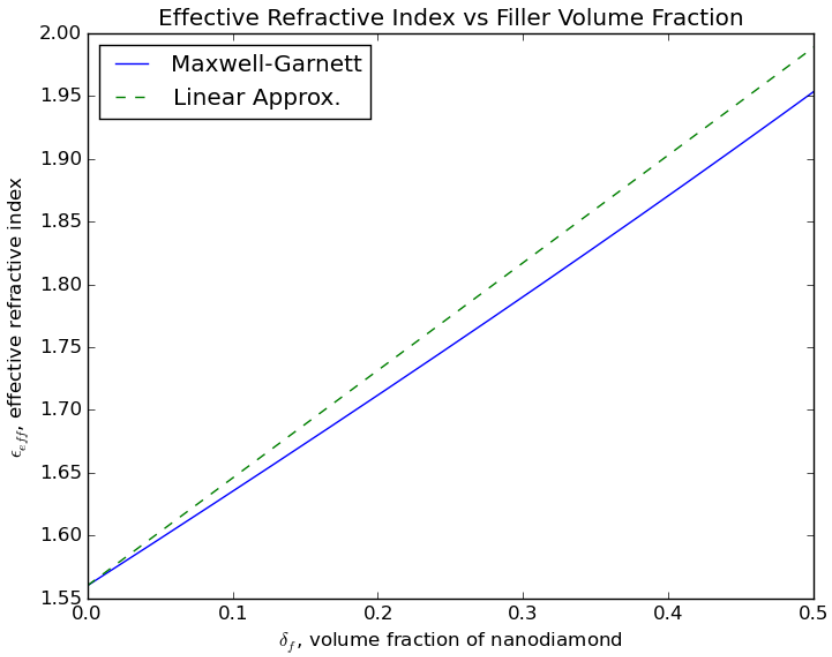

Figure 2.2: Variation of effective refractive index for a composite of Norland Optical Adhesive #61 and nanodiamond for loadings up to 50% volume. The index notably departs from a simple linear approximation.

The most common diamond synthesis process doesn't aim to produce optical quality diamonds, but industrial abrasives for polishing. By detonating a carbon-rich explosive in a confined volume, the pressure, temperature, and carbon needed for diamond formation are all present. The resulting soot is a deep grey color and contains diamonds that can be just a few nanometers in size. Unfortunately other allotropes of carbon, as well as trace metals from the pressure vessel, will inevitably be present. It was our initial assumption that removing these contaminants would produce a pristine colorless diamond which could be used as a composite filler material, but in the end additional processing was required.

The diamonds produced by this detonation process are often called detonation nanodiamonds, or DNDs, and are typically on the order of 1 to 10 nanometers in diameter. This is a suitable size for an optical composite material as particles much

smaller than the wavelength of light result in Rayleigh scattering. The equation for expressing the scattered intensity from a spherical particle is given in (2.3) below[55], where I is the scattered intensity, I_0 the incident intensity, θ the scattering angle, R the distance to the particle, n the refractive index of the particles, λ the wavelength of the light, and d the particle diameter. Averaging over all scattering angles yields the scattering cross-section (2.4), which when multiplied by the number of particles per unit volume yields the fraction of light scattered.

$$I = I_0 \frac{1 + \cos^2 \theta}{2R^2} \left(\frac{2\pi}{\lambda}\right)^4 \left(\frac{n^2 - 1}{n^2 + 1}\right)^2 \left(\frac{d}{2}\right)^6 \tag{2.3}$$

$$\sigma_s = \frac{2\pi^5}{3} \frac{d}{\lambda^4} \left(\frac{n^2 - 1}{n^2 + 1}\right)^2 \tag{2.4}$$

The magnitude of the Rayleigh scattering cross-section goes with the particle diameter to the sixth power, so suitably small particles can result in negligible amounts of scattering even for large particle loadings.

2.2 Methods

2.2.1 Removal of Impurities and Intermediate Characterization

The process for removing the impurities from nanodiamond requires several steps; a schematic workflow is presented in Figure 2.3. A nanodiamond powder was obtained from Sigma-Aldrich, with a reported average size of 10nm. 500mg of the nanodiamond was thermally cleaned at 450 °C with a half-hour ramp and one hour hold in air, as this has been shown to remove the majority of non-diamond carbon from the material[5, 60]. It was then allowed to cool for roughly an hour in ambient temperature air.

In order to remove metal impurities from the nanodiamond, two acid-washing treatments were performed. The first acid-wash was done with 30mL of HCl, also from Sigma-Aldrich, at 120° C for 1 hour. The heating was done on a hot-plate stirrer under a fume hood in a clean room, and the mixture was stirred at 1100

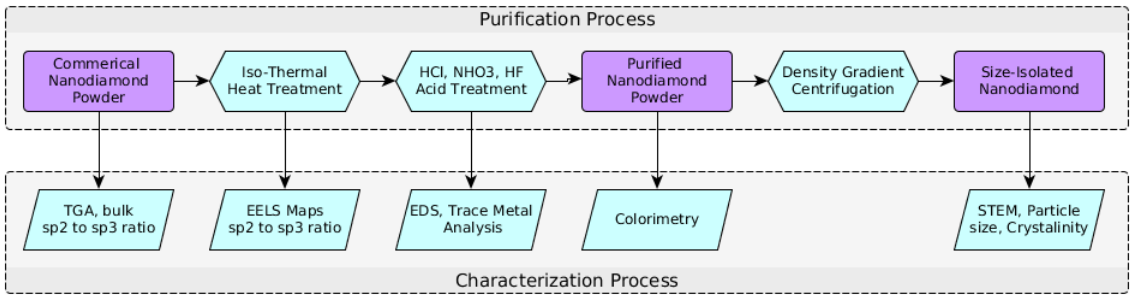

Figure 2.3: Workflow for purification and characterization of nanodiamond. The top row describes the processing required to produce the final nanodiamond product, while the bottom row describes the characterization methods employed at each step.

rpm. Afterward, deionized water was used to rinse the resulting mixture from the flask, and it was allowed to settle for several hours. The supernatant liquid was removed and the solid was moved into several (between 10-12) small centrifuge tubes for rinsing. Deionized water was added, and the tubes were agitated for 5 minutes. The dispersed mixture was then centrifuged at 7500 rpm for 20 minutes. This process was repeated, exchanging supernatant for deionized water, until the pH had returned to neutral. It is during this centrifugation process that the exceptional blue layer appeared in each of the small test tubes just as the pH approached neutral, as shown in Figure 2.4.

Throughout the purification process several characterization methods were used to monitor the efficacy of each step of removing the targeted species. Just as the specifics of the cleaning process, we will address the details of the characterization methods in turn.

Thermogravimetric Analysis

Thermogravimetric analysis (TGA) is a thermal analysis method capable of identifying first and second-order phase changes as well as relative compositions in materials that experience oxidation or decomposition at increased temperature. The measurement is performed by sensitive monitoring of the mass of the material sample under test as it undergoes predetermined temperature changes. For our

Figure 2.4: The blue and grey layers as the first appeared during the rinsing process.

system, TGA was used to determine the ratio of sp^2 bonded (graphitic) carbon to sp^3 bonded (diamond) carbon. This was performed before and after the isothermal cleaning step to determine efficacy. A ramp rate of 0.5 °C/min was found to be sufficient for consistency between samples and vendors, and we did not observe any significant differences between nanodiamond isothermally cleaned in air and nanodiamond isothermally cleaned in an oxygen tube furnace. Fourier transform infrared spectroscopy (FTIR) was used both to confirm the action of the oxidation cleaning as well as to determine functional groups, adsorbed molecules, and impurities on the surface of the carbon. The primary peaks monitored were at $1600cm^{-1}$, indicative of sp^2 hybridized carbon, and at $1800cm^{-1}$, indicating sp^3 hybridized carbon.

The other features in the FTIR spectra of as-received powders are related to $C = O$ (1740-1757 cm^{-1}), $C - H$ (2853-2962 cm^{-1}), and O-H vibrations (3280-3675 cm^{-1} stretch and 1640-1660 cm^{-1} bend), which can be assigned to $-COOH$, $-CH2-$, $-CH3$, and $-OH$ groups of chemically bonded and adsorbed surface species. The comparison of FTIR spectra of purified and as received powders reflects the conversion of a variety of surface functional groups into their oxidized derivatives. After thermal oxidation, $-CH2-$ and $-CH3$ groups are completely removed while the number of $-OH$ groups is increase. In addition it was observed that the $C = O$ vibrations are upshifted by 20-40 cm^{-1}, indicating a conversion of ketones, aldehydes, and esters on the surface into carboxylic acids, anhydrides, or cyclic ketones.

Electron Energy Loss Spectroscopy

By exposing a material to a beam of electrons with a very narrow distribution of kinetic energies and measuring the kinetic energies of the post-interaction electrons, one can back out the elemental composition of the material under test. This is due to the fact that the removal of inner-shell electrons requires a different amount of energy for each atomic species, and thus the energy difference imparted by interaction indicates the species present. This method is known as electron energy loss spectroscopy (EELS), and is typically built on to an existing electron microscope. For our material, spectra were recorded using a scanning transmission electron microscope (JEOL 2010F), operated at 200 kV, equipped with TEM / STEM and Gatan high-resolution GIFT EELS detectors.

Energy-Dispersive X-ray Spectroscopy

By focusing high-energy x-rays onto a material sample, one can cause inner-shell electrons to be ejected from the atoms. When this happens, a higher-energy bound

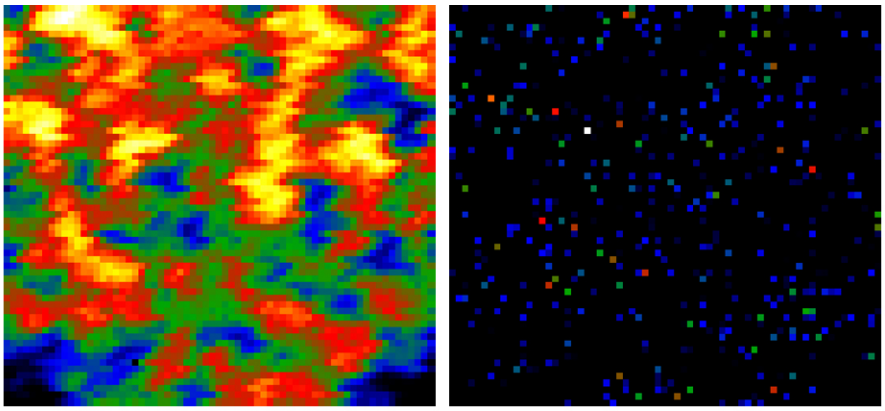

Figure 2.5: Reconstructed maps of the distribution of sp^3 bonded carbon (left) and sp^2 bonded carbon (right) of a sample after isothermal oxidation. Amplitude is normalized, imaged area is 60 nanometer square.

electron can drop into the now vacant state, releasing a photon with energy equal to the difference in this process. By detecting the energies of these photons one can determine the atomic species present. This is called energy dispersive x-ray analysis (EDAX), and is capable of detecting very small impurities. The EDAX spectra were measured with a Hitachi S-3400 after each of the acid-cleaning steps to determine the efficacy and extent of the removal of trace metals. Kα^* energy between 0 and 11 keV was measured, permitting the detection of atomic species with atomic number up to 33. The spectra are presented in Figure 2.6, and show a clear reduction in the number of detected contaminant species. After the HF cleaning, there are no apparent atomic species except oxygen and carbon.

2.2.2 Isolation of Size Fractions

Density gradient centrifugation is a method by which a solution containing suspended particles may be separated into fractions of narrower size distribution and known density. As the particles match the density of the level they remain at after sufficient centrifugation, this is referred to as isopycnography. This is achieved by preparing a group of mutually miscible solutions of differing densities, and carefully

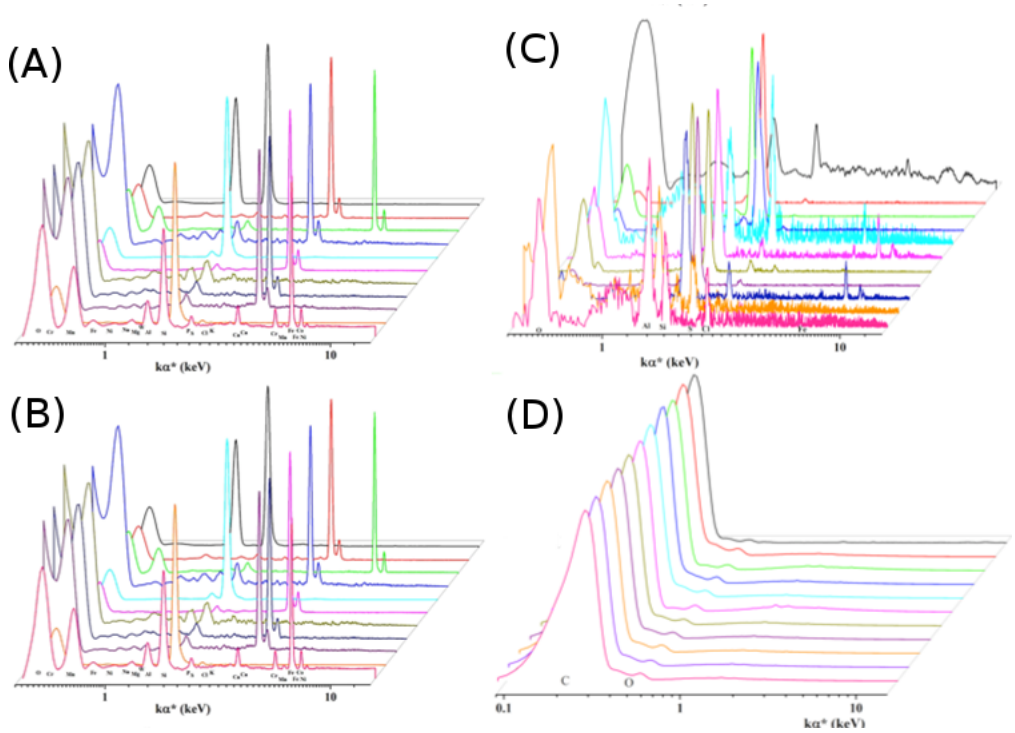

Figure 2.6: Comparison of EDAX spectra for nanodiamond (A) as received, (B) iso-thermally heated, (C) after HCL treatment, and, (D) after HF treatment.

creating a layered stack of progressively lower density within a single centrifuge tube. A photograph of such a stack used in this work is presented in Figure 2.7. In order to attain a linear relation between tube-depth and liquid density, the linear stack is briefly centrifuged (for our work, 20 minutes at 3500 rpm was sufficient). The solution in question is carefully introduced into the density gradient by syringe, and centrifuged once more. If the solution is sufficiently dilute, this will allow larger particles to move down the length of the gradient until their density is matched by the solution around them, while smaller particles do the opposite. This method was first pioneered in the 1930s for isolation of cellular organelles and large biological molecules [9], and has since seen widespread use in biology and physical chemistry, and has been successfully applied to nanodiamond particles in the past [58].

We chose to use OptiPrep density gradient medium as it provided access to

the expected range of densities and was compatible with surfactant-treated particles. A continuous density gradient was realized from discrete solutions by briefly centrifuging the discrete stack of layers.

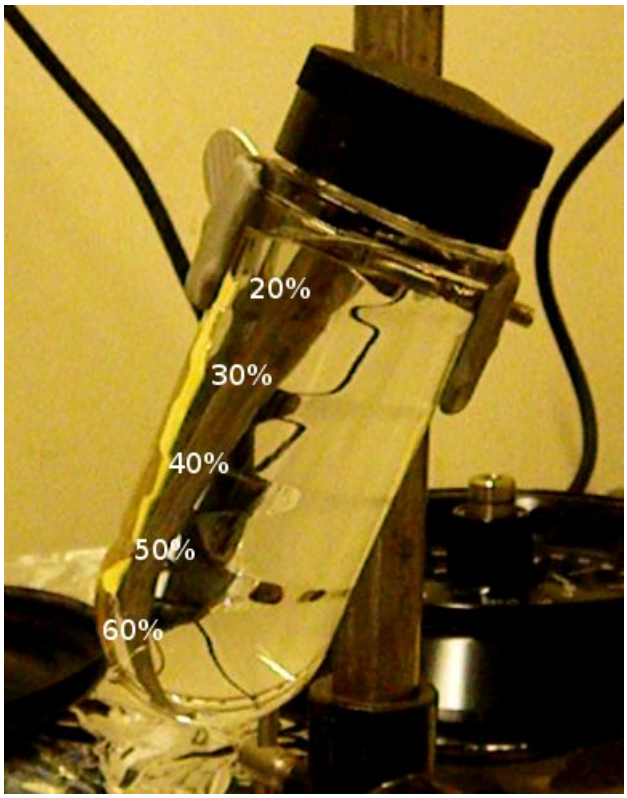

Figure 2.7: Photo of a six layer step-density solution before linearization. The boundaries between the layers are visually apparent due to the differences in refractive index. The labels indicate the relative concentration of density gradient media in dionized water.

2.2.3 Preparation of the Density Gradient

A linear density gradient was prepared using 60% OptiPrep in deionized water, with relative density gradient media concentrations of 60%, 50%, 40%, 30%, and 20%. One beaker was prepared for each ratio and stirred for 15 minutes to ensure complete mixing. 14 ml of each solution, in order of decreasing density, were carefully added to a 70 ml centrifuge tube via syringe. The resulting structure was centrifuged at 3500 rpm for 20 minutes, resulting in a linearized density profile

within the tube. A sample of nanodiamond, thermally cleaned and acid treated as outlined in the previous section, was agitated in deionized water with 1 g sodium cholate surfactant. The mixture was then sonicated briefly and introduced into the linear density gradient via syringe. The density gradient was then centrifuged at 3500 rpm for 99 minutes. The small amount of material had spread out to form a large cloud, and liquid was extracted from three regions within the density gradient and centrifuged separately. The isolated solids from each were collected and dissolved in a small amount of deionized water. UV-Visible transmission spectra were taken from these samples as an initial attempt to quantify the scattering and absorption properties of each fraction.

The material from the layer with the lowest density was isolated, and fractioned utilizing a secondary density gradient. This gradient was comprised of 10 layers with density gradient media concentrations of 60%, 40%, 36%, 32%, 28%, 25%, 21%, 17%, 14%, and 10%. The smaller density difference of the lower density layers was chosen to more widely spatial separate small differences in density. The gradient was linearized, the previously isolated material was introduced to the center layer, and it was centrifuging to disperse the material. Several scanning transmission electron microscopy (STEM) micrographs were also produced for each fraction.

2.3 Results and Characterization

The results of UV-Vis transmission spectroscopy are shown in Figure 2.8 below. Beyond normal Rayleigh scattering, there are no notable spectral characteristics. This suggests that the mean particle size must be different in the bulk as compared to the blue layer, and this was borne out by subsequent STEM imaging. The images produced by STEM performed on both the isolated blue layer material as well as the isolated gray bulk material are presented in Figures 2.9 and 2.10. The accelerating voltage used was low enough to not cause instability within the particles [30].

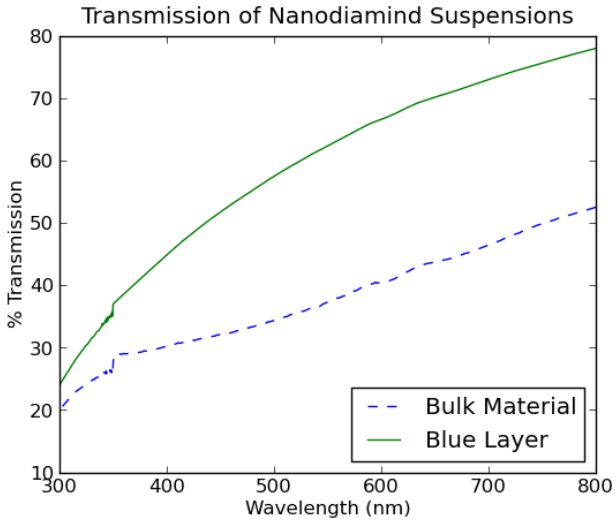

Figure 2.8: Transmission spectra from the bulk and blue nanodiamond material in deionized water.

It is clear that both sets of micrographs show agglomeration, but there is an order of magnitude difference in the scale of this agglomeration between the two based upon the mean agglomerate cross-sectional area, with blue layer possessing an average aggregate area of 4,842 nm^2, while those in the bulk layer averaged 40,680nm^2. Similarly, in the blue material micrographs the particles are thinly agglomerated into low-density structures lying mostly in the plane, while the bulk material appears to agglomerate into higher density groups with multiple layers of particles apparent within each agglomerate. The individual nanoparticles in each set showed the structure typical of detonation-type nanodiamond[38].

The region containing the proportionally larger blue layer corresponded to the smallest effective particle size. This smaller particle size leads to a blue color in reflection (yellow-orange in transmission) due to Rayleigh scattering off of the particles. In the gray nanodiamond the effective particle size was large enough that the strong spectral features in the visible were suppressed. While the agglomeration behavior and aspect ratio in solutions of this type is strongly dependent upon pH[29], the particle size was a driving factor in determining the color of the material. The next step was to further fraction the blue material into narrower size distributions.

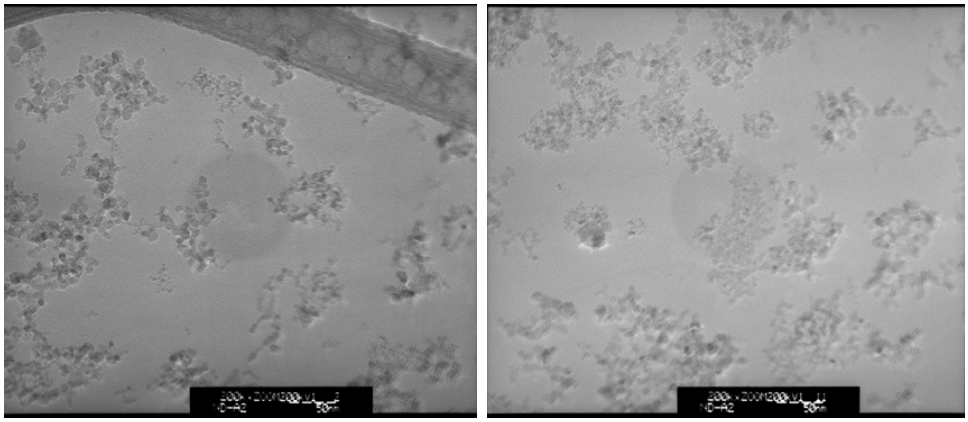

Figure 2.9: Scanning TEM micrographs of blue-colored isolated nanodiamonds

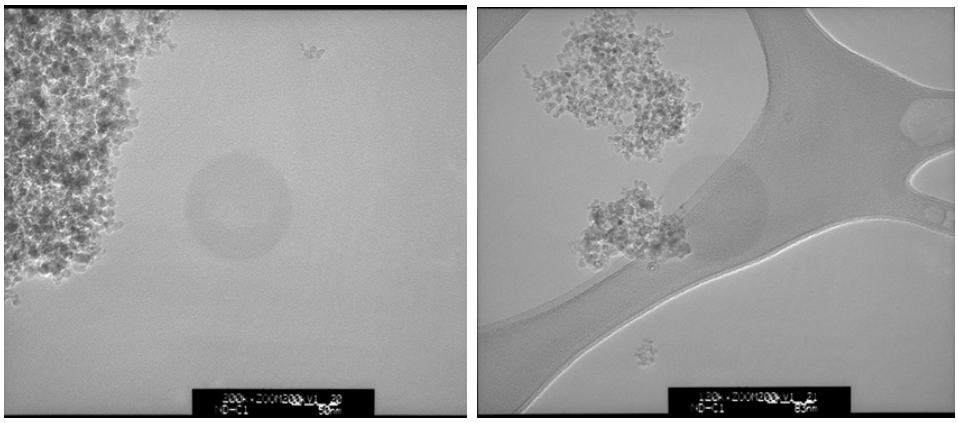

Figure 2.10: Scanning TEM micrographs of grey-colored bulk nanodiamonds

The second size-selection process resulted in ten fractions, corresponding to the ten densities selected for the gradient. The lowest-density fraction, when separately centrifuged produced a very small amount of detectibly white nanodiamond powder. The remaining nine fractions appeared blue-grey, but had insufficient material volume for additional determination.

2.4 Conclusions

Optical quality nanodiamond particles that are highly crystalline and free of impurities were produced from commercially obtained detonation nanodiamond. This was done through a combination of thermal oxidation, acid washing, and density gra-

dient centrifugation. The removal of sp^2 bonded carbon was confirmed with TGA, while EELS and EDAX were used to assess the removal of metallic impurities. STEM micrographs were taken of the fractioned nanodiamond revealing previously unobserved primary particles of highly crystallinity with an average diameter of 2nm.

CHAPTER 3

Self-Assembled Magneto-Optic Nanocomposites

3.1 Background

In the previous chapter we addressed a single component of a hybrid system. Purified nanodiamond is a component that can contribute unique properties to any number of compatible host materials. While this approach is valid, a composite can derive even greater benefits by exploiting both the properties of the filler as well as those of the matrix. In this way we approached a system combining a block co-polymer host with strongly interacting magnetic nanoparticles to attain propeties neither system could produce in isolation.

Given the nearly inert nature of many common materials under a magnetic field, one often neglects the effects of those fields upon light. However, many materials depart sharply from this regime, strongly linking the magnetic field to the properties of propogating electro-magnetic radiation. While there are several distinct optical effects created by magnetic fields, we are focused on perhaps the simplist: Faraday rotation. Through this eponymous effect, first observed by Micheal Faraday in 1845, an applied or intrinsic magnetic field can cause the refractive index of a material to be different for left- and right-circularly polarized light[18]. The practical impact of this effect is that the plane of polarization of linearly polarized light will be rotated by a predictable amount upon passing through a given material. As shown in 3.1, this rotation is directly proportional to the magnitude of the component of the applied field B parallel (or anti-parallel) to the light propagation, the interaction length L, and a material property called the Verdet constant, V, with units of degrees per Tesla-meter.

$$\theta = VBL \tag{3.1}$$

This effect is interesting, as essentially all materials possess a non-zero Verdet constant, but the magnitude of these constants vary over several orders of magnitude. For example, N-BK7, a common glass for commerical optical components, possesses a Verdet constant of $150^\circ\,\mathrm{T}^{-1}\,\mathrm{m}^{-1}$ at 830nm[61], whereas terbium gallium garnet (TGG), a commerically relevant inorganic optical crystal, possess a Verdet constant of -3724° $\mathrm{T}^{-1}\,\mathrm{m}^{-1}$ at the same wavelength[7]. Here the negative sign indicates a material that rotates the polarization in the opposite direction. Under normally encountered fields, many materials could cause a polarization change small enough to be obscured by other sources of erorr, but for some one can obtain a rotation of 90° or more, for reasonable thicknesses.

This effect can be utilized to perform several functions, as presented in Figure 3.1. Paired with a polarization analyzer, one can determine the magnetic field at a given point in space by monitoring the recieved intensity. Similarly, one can modulate the intensity by applying a known field in the same configuration.

The third application, shown in Figure 3.2, utilizes the most notable feature of this effect; it is non-reciprocal. This means that the sense of the rotation of the plane of polarization does not depend on the direction of propagation. As light passing through in either direction is rotated by θ, a double-pass yields 2θ rather than perfect cancellation, as would occur for a half-wave plate, as an example. A stack consisting of a linear polarizer, a length of magneto-optic material under sufficient field to produce a 45° rotation, and a second linear polarizer oriented at 45° will produce what is called an optical isolator. Light entering from the "front" will by attenuated until only light at 0° remains, be rotated to 45°, and pass the second analyzer with negligable attenuation. Meanwhile, light entering from the "back" will be attenuated until only 45° light remains, be rotated an additional 45° in the same direction to 90°. This

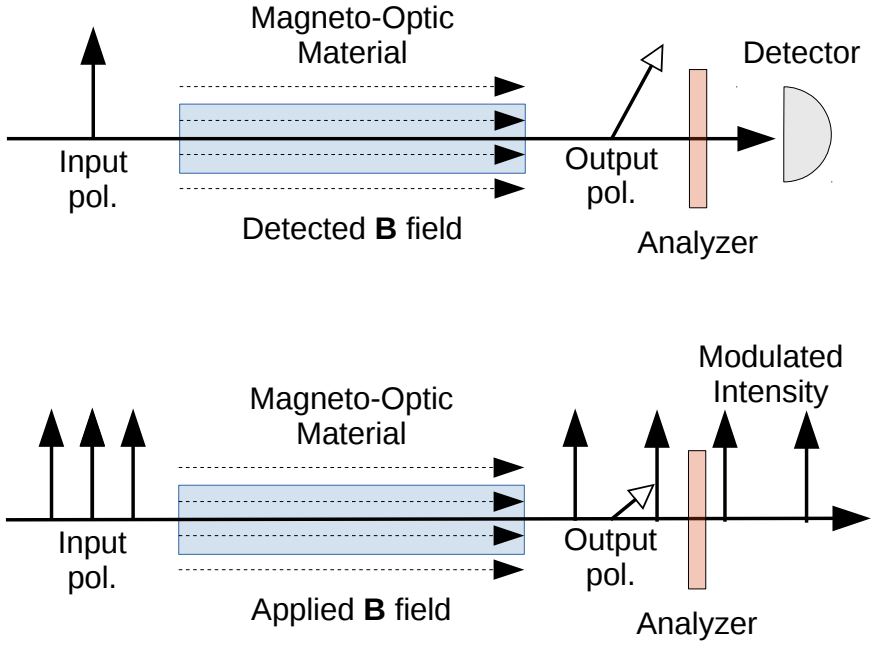

Figure 3.1: Example applications of Faraday rotation for sensing magnetic fields (top) and modulating intensity (bottom). Hollow-point arrows do not lie in the plane of the page.

orthogonal state will be almost entirely attenuated by the first analyzer in the stack.

While optical isolators are only one application, due to their necessity in optical telecommunications networks, they are presently the most commercially significant application for magneto-optically active material. With a very large Verdet constant and good transparency, permitting the use of smaller applied fields and interaction lengths, TGG is the most commonly used material for optical isolators[2]. The key issue for TGG is common among inorganic optical crystals, namely they are expensive to fabricate, sensitive to damage, and difficult to package and integrate into a system. A composite material holds the potential to combine the necessary magneto-optical properties of a filler with a polymer host, providing a pathway to a material with a large Verdet constant that can be easily bulk-processed and packaged.

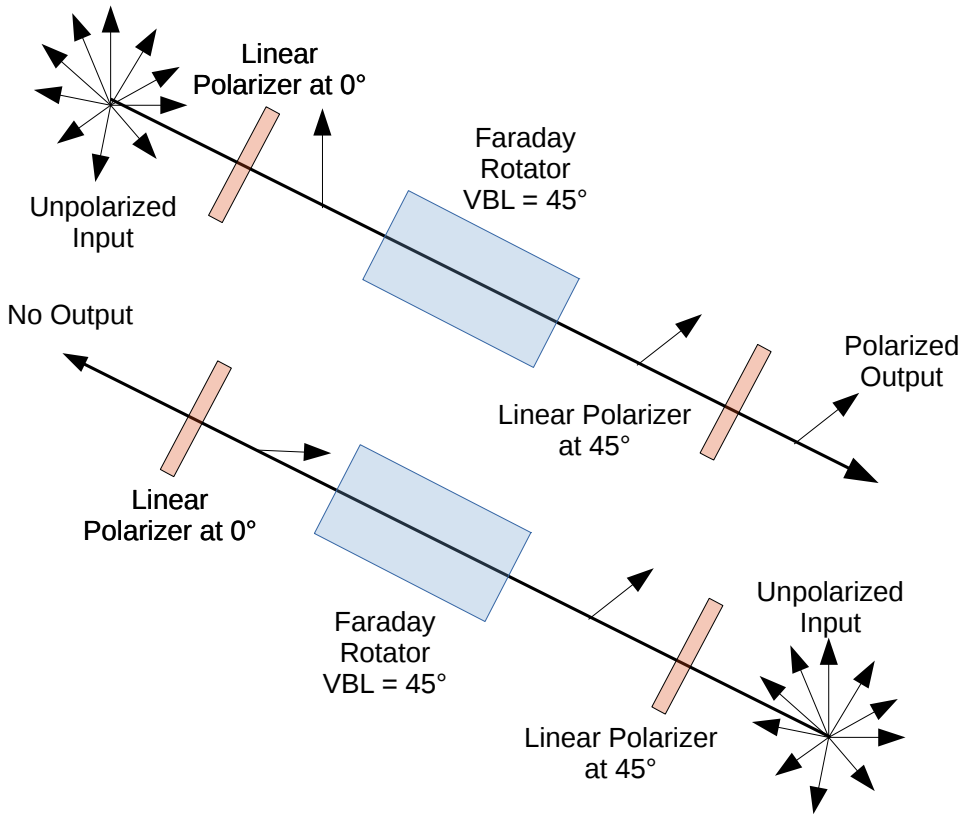

Figure 3.2: Schematic function of non-reciprocal Faraday rotation used to produce an optical isolator with light propogating in the forward (top) and backward (bottom) directions.

3.1.1 Materials Selection and Scope

How a material responses to an applied magnetic field can be seperated into diamagnetic, paramagnetic and ferromagnetic classes. Diamagnetic materials create induced magnetic fields in the opposite direction of the applied field, paramagnetic materials create induced fields that are parallel to the applied field, and ferromagnetic materials retain a permanent internal magnetic field capable of strong interactions with applied fields. The differences between these classes can be encapsulated in their magnetic susceptibility, χ_m, which is the dimensionless material constant relating the degree of magnetization, $\mathbf{M}$, to the applied magnetic field, $\mathbf{H}$ (both having units of ampere per meter). This relation is shown in (3.2). A positive value of χ_m indiates a paramagnetic material, one that strengthens the magnetic field, while

a negative χ_m corresponds to a diamagnetic material that opposes an applied magnetic field. Ferromagnetic materials have postive values of χ_m, but retain additional magnetization even in the absence of applied fields.

$$\mathbf{M} = \chi_m \mathbf{H} \tag{3.2}$$

Glasses and other diamagnetic materials display weak magneto-optic response and little dependence on temperature, due to the partial cancellation of the induced magnetic field and the external one. Nanoparticles containing iron or cobalt, if their core diameters are less than 20 nm, have been observed to be paramagnetic[3], and will be attracted to applied magnetic fields. In addition, they may lose their magnetization due to thermal changes. The combination of large positive susceptibility and strong thermal response led to the selection of these particles as our field-sensitive filler. In particular, for the filler material we selected iron-platinum (FePt) nanoparticles.

FePt provides excellent magnetic and chemical stability, and has found applications in high-density magnetic storage[53] and bio-sensing[47]. Synthesis and surface modification of FePt is routine, and produces size controlled nanoparticles at sizes smaller than 10 nm. This level of control allows us to investigate the unique size dependent properties of these particles, especially the transition from paramagnetic to ferromagnetic behavior. Despite the breadth of applications, little effort has previously been made to utilize the magneto-optic effects of these particles.

For the host material a block co-polymer, polystyrene-b-poly (2-vinyl pyridine), abbreviated as PS-b-P2VP, was chosen. This polymer is one of a family of nanostructured block copolymers capable of forming composites containing functional fillers such as our nanoparticles. Similarly these polymers have been used to host liquid crystals and organic small molecules in a push toward next generation materials with improved electronic and optical qualities [51, 10]. Linear block copolymers have exhibited the ability to direct surface modified inorganic NPs arrays

interactions between nanoparticles surface ligands and specific co-polymer blocks. This block co-polymer host provides a template for integrating our nanoparticles into a nanostructures magneto-optic material. Most significantly, this host material permits the creation of large-area devices, and even roll-to-roll processing of the final composite material.

We collaborated with Professor James Watkin's Polymer Science Group at the University of Massachusetts Amherst, and they were able to prepare a variety of films for us to characterize. With mean particle size varying from 2nm to 12nm, weight-loading of the particles in the host polymer varying between 0.1% and 25%, and using characterization wavelengths between 845nm and 1550nm, we performed a systematic study of the Verdet constants. Additionally, atomic-force microscopy (AFM) was employed to investigate the nanosctructuring of the composite material directly and shed light on the connection between particle loading, size, and resulting structure and properties.

3.2 Experimental

3.2.1 Nanoparticle Characterization

The FePt particles incorporated into the composite materials were characterized by our collaborators. The core diameters of the nanoparticles were characterized by transmission electron microscopy (TEM) on a JEOL model 2000FX operating at 200 kV. The samples were prepared by dropping a dilute nanoparticle solution on a thin carbon film supported by a copper grid. Images containing 300-400 particles were analyzed in ImageJ, a scientific image analysis program, to provide the size distribution and histograms shown in Figure 3.3. The TEM diffraction images were obtained using the same procedure, subtituting a more concentrated solution of particles. The weight fraction of the metal core was measured by thermogravemetric analysis (TGA), using a TA Instrument model Q500. Data was taken from from 20°C to 800°C at 10°C per mintue in air. The nanoparticle

crystallinity was confirmed by x-ray diffraction (XRD) on a Panalytical X-pert X-ray Powder Diffractometer, as shown alongside the TEM images in Figure 3.4. The initial four batches of FePt NPs were obtained with average core diameters of 1.9, 4.9, 5.7 and 9.3 nm, respectively, with narrow distributions, as seen in Figure 3.3. The spherical to cubic shape transition is observed with increasing size of NPs.

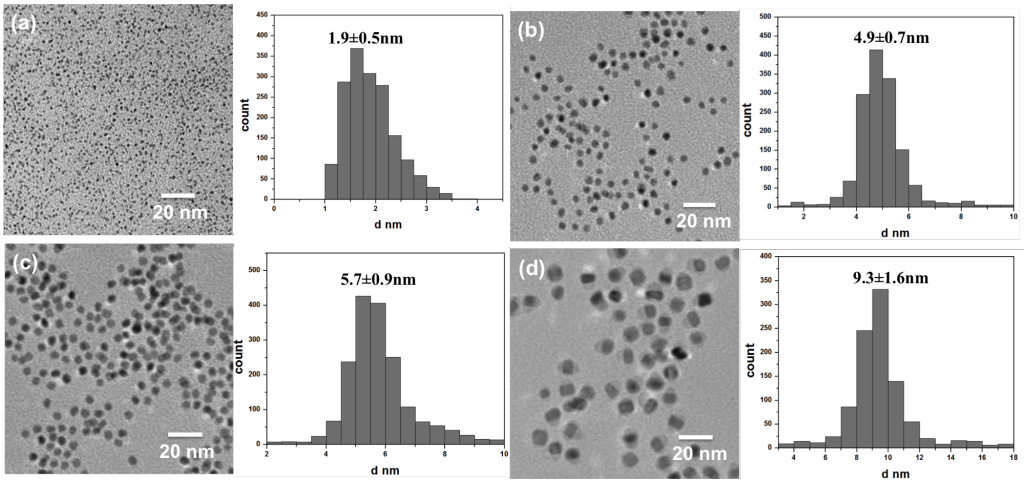

Figure 3.3: TEM images of gallic acid capped FePt nanoparticles and corresponding size distributions, average core diameter (a) 1.9 nm, (b) 4.9 nm, (c) 5.7 nm and (d) 9.3nm.

3.2.2 Composite Material Characterization

Film Thickness

The composite films themselves were characterized and tested at the University of Arizona. The film thicknesses were determined by contact profilometry using a Veeco Dektak 150. There were some issues with achieving sufficient uniformity in the film thickness; these departures were occasionally substantial, with up to 50% variation in the thickness across a single line-scan. This variation is not unexpected as they were fabricated by drop-casting. This fabrication method involves allowing individual drops of a solution of particles, polymer, and solvent to evaporate on a substrate to build up a film, which can produce suitably thick films but yields far

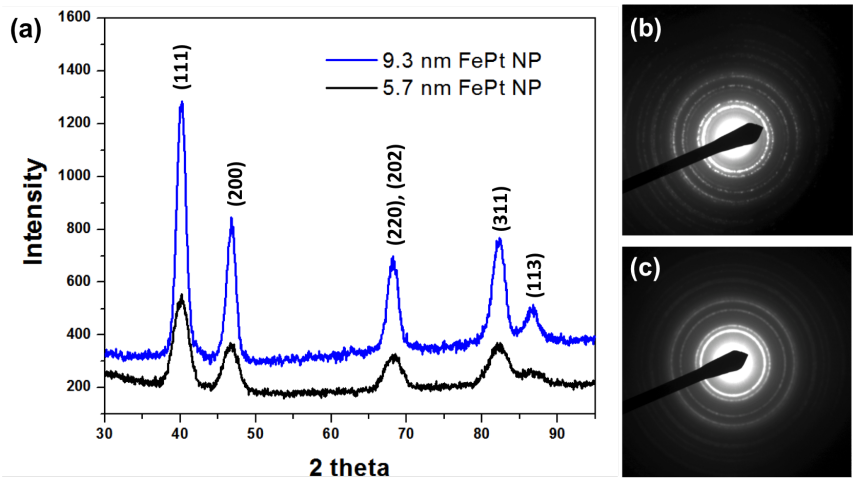

Figure 3.4: X-ray diffraction data indicating the FePt nanoparticles posses a face-centered cubic crystal structure (left) and the TEM diffraction images indicating a high level of crystalinity (right).

worse uniformity than spin coating or blade coating. Given that any error in the thickness measurement directly impacts our calculated Verdet constant, we chose to measure only the 0.9 mm square segment of film actually used in the rotation measurements. In addition, for each sample three parallel scans were taken across the area the beam would pass through, and those thicknesses and uncertainties were used in the Verdet constant calculation.

Faraday Rotation

The Verdet constants were measured in a two-pass AC-driven apparatus using a NewFocus Nirvana 2017 auto-differential detector with efficient common-mode noise cancellation. This detector, employed in conjunction with a lock-in amplifier, allowed for accurate measurement of small Faraday rotations. A polarization control consisting of a half-wave plate and a high extinction-ratio linear polarizer prepared the light in a known polarization state. After a non-polarizing beam splitter (NPBS), the light is passed through the sample twice, yielding a rotation of the linear polarization state of 2θ, where θ is directly proportional to the sample

thickness, applied magnetic field, and Verdet constant. The light is then spatially separated into vertical and horizontally polarized components (often denoted s and p) by a Wollaston prism, focused by a coated singlet lens, and detected by the auto-differential detector. The setup described is shown schematically in Figure 3.5.

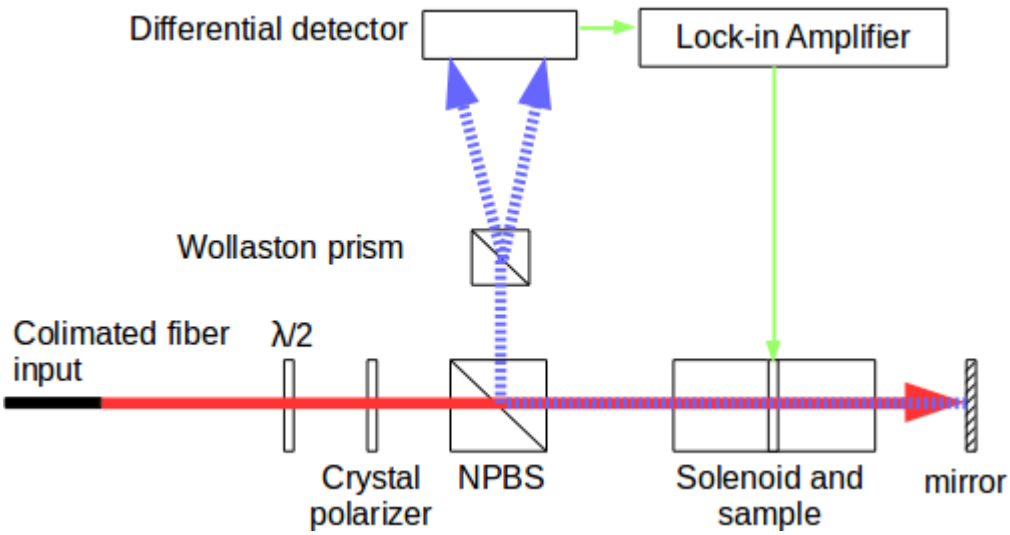

Figure 3.5: Schematic drawing of AC Faraday rotation measurement system. The dashed blue line represents the second pass through the sample.

The two detectors are specified as reference and signal, with the detected powers being denoted P_{ref} and P_{signal} respectively. When the detector is set in 10X mode, the mode used during our measurements, the two signals measured at the lock-in amplifier (specified as DC and AC) can be calculated from the detected powers as shown in (3.3), wherein g is the internally adjusted reference channel gain and R is the detector responsivity at the wavelength used. The lock-in amplifier serves to both detect the signal as well as drive the amplifier for the solenoid coil at 375 Hz. Several hundred measurements are averaged at each applied field value to minimize the heating effects and account for the time constant of the lock-in amplifier.

$$DC = 10RP_{signal}, \quad AC = 1000R\left[P_{signal}(f) - gP_{ref}(f)\right] \tag{3.3}$$

As the Faraday rotation determines the ratio of the signals, from these values we can calculate the total rotation and in conjunction with the measured thickness, the Verdet constant. Explicitly this means one must divide the AC signal by twice the DC signal, divide by 100 to account for the detector settings, divide by two to account for the double-pass configuration, and then convert the value from radians into degrees. These operations produce the conversion given in 3.4.

$$\theta = \frac{180^\circ}{\pi}\frac{AC}{2DC}\frac{1}{100}\frac{1}{2} = \frac{-57.296AC}{800DC} \tag{3.4}$$

At each wavelength the Faraday rotations contributed by the 1mm thick glass substrate had to be accounted for. The Verdet constant of a bare glass substrate was measured at each wavelength as calibration; the values were found to agree well with existing literature[24, 7] and are provided in Table 3.1. Parsing the raw data from the lock-in amplifier was an involved task, and the Python script written to handle this translation is included in Appendix A.

Wavelength (nm)	Verdet Constant (deg/T-m)
845	146.8
980	104.0
1310	74.0
1550	39.1

Table 3.1: Measured Verdet constants for glass substrates

Material Microstructure

As will be discussed in the results section, we observed a non-linear change in the magneto-optic response as a function of nanoparticle loading. This indicated that some change was occurring in the microstructure as more and more particles were added to the composite. Given the relatively large thicknesses of the material (approximately 10µm) and our inability to reliably separate the films from the glass substrate without damaging them, we chose atomic-force microscopy (AFM) to interrogate the surface structure of the films. In AFM a sample is moved in a plane beneath a cantilever using piezo-electric elements. This cantilever has a very

small tip that interacts with the surface through van der Waals or other forces, based on the tip material and desired characterization. Laser light is reflected off the back of this cantilever. In "static mode", the displacement of this beam on a four-quadrant detector becomes the signal, while in "tapping mode" the response of the cantilever to oscillation as a function of frequency is monitored, and changes in this characteristic provide the signal. In this way we can build up a spatial map of a given property of the surface by testing the degree of interaction at many points. The two key benefits of AFM are resolution and flexibility. The type of interaction used isn't subject to the diffraction limits of optical and electron microscopy, and the tips can be made exceedingly small, and thus the sampled area for each data point; resolutions under a single nanometer are possible. The tips themselves can be made magnetic, possess an electric potential difference, or even attached to a reactive molecule to probe magnetic, electric, and even chemical properties of a sample.

We used a Veeco Innova atomic force microscope equipped with a Nanodrive controller and a standard platinum-iridium tip to measure the film surface topologies in tapping mode. These images are presented and discussed in the following section.

3.3 Results

3.3.1 Verdet Constants

The calculated values for the tested samples are provided in Table 3.2. It is immediately notable that several of the samples surpass the Verdet constants provided by TGG (e.g. TGG has a Verdet constant of about -3200° m^{-1} T^{-1} at a wavelength of 845nm), almost by a factor of 20 in the case of the highly loaded 4.8nm FePt films.

Having tested samples with varied particle loading, particle size, and operating wavelength, we were able to visualize this data in several ways. As expected for paramagnetic materials, the Verdet constant for all the tested systems dropped reliably as the inverse square of the wavelength[14], which is easily seen in Figures

	845nm				980nm			
wt% / NP dia.	2.0nm	4.8nm	5.4nm	10nm	2.0nm	4.8nm	5.4nm	10nm
0.1%	-38160	-52467	-28092	-31810	-29555	-35234	-21564	-21846
0.5%	-34294	-40910	-52496	-29972	-27054	-29521	-37098	-20526
1.0%	-36191	-32677	-45117	-31753	-28736	-20523	-29924	-22695
2.5%	-32019	-37066	-48314	-44214	-25648	-27009	-28046	-32675
5.0%	-43892	-47940	-47901	-53387	-33014	-34566	-33014	-38339
7.5%	-29923	-55141	-48762	-40032	-25806	-41307	-32003	-23468
10.0%	-36113	-62676	-46976	-43929	-29126	-47007	-32931	-31793
	1310nm				1550nm			
wt% / NP dia.	2.0nm	4.8nm	5.4nm	10nm	2.0nm	4.8nm	5.4nm	10nm
0.1%	-10858	-22725	-12147	-13486	-10858	-13723	-3712	-5438
0.5%	-9754	-17967	-22047	-11955	-9754	-9566	-6670	-6364
1.0%	-9770	-14540	-19342	-14247	-9770	-9125	-5698	-5809
2.5%	-9029	-16591	-20731	-19346	-9029	-10122	-6199	-8023
5.0%	-11414	-20963	-20572	-22521	-11414	-12620	-6533	-7847
7.5%	-9077	-23312	-21013	-17651	-9077	-14766	-6750	-6676
10.0%	-10189	-27855	-20797	-18918	-10189	-17363	-7667	-7008

Table 3.2: Measured Verdet constants in degrees per Tesla-meter. The given weight percentages include the capping layer of gallic acid.

3.6 and 3.7. In addition, those figures show a saturation-like behavior, beyond which additional particles do not appear to increase the Verdet constant of the composite. This behavior is more easily seen when a larger cross-section of the data is presented on a single plot. At this point, a distinction becomes necessary; each particle size, when capped with gallic acid has a different ratio of FePt to gallic acid, and thus converting the weight percent of particles into true weight percent FePt must be done carefully. The micrographs presented in Figure 3.3 were used by our collaborators to back out the fraction of FePt for each family of samples tested, and these scale factors are presented in Table 3.3. When plotted together against actual fraction of FePt, as shown in Figure 3.6, it is apparent that the particles 4.8nm and smaller have not yet reached the saturation behavior seen in the other samples.

When this was seen, the decision was made to see how far the composites with 4.8nm FePt nanoparticles could be pushed. Four additional films were delivered with FePt fractions (not including the capping agent) of 10, 15, 20, and 25%. Given

Avg. Diameter	Fraction FePt	Loadings Range
2.0nm	21%	0.021% - 2.1%
4.8nm	72%	0.072% - 25.0%
5.4nm	68%	0.068% - 6.8%
10nm	76%	0.076% - 7.6%

Table 3.3: Ratio of FePt to capping agent for each particle size

the predictable nature of the wavelength variation and time-intensive nature of realignment of the measurment aparatus, these last samples were measured only at 1310nm wavelength. The extended behavior is presented in Figure 3.8, and indicates a sharp change in behavior between 7.2 and 10%.

With samples far into the saturation regieme, at either edge, and far below, we had a great opportunity to investigate the structural causes for this reversal. AFM images taken from the films with 5.4%, 7.6%, 10%, and 15% loadings of 4.8nm FePt are presented in Figure X below (**We have these images, but I'm presently attempting to obtain the actual files from Palash, who is presently abroad**). Films at or beyond saturation show distinct long-range organization of the nanoparticles into distinct domains, whereas the films below the threshold show very little order. This indicates that a screening or anti-cooperative effect is taking place, reducing the effectiveness of the particles are they become capable of forming into larger aggregates. Given the larger active volume of the larger particles, it makes sense that they encounter this cutoff at much lower particle loadings.

3.4 Conclusions

Combining self-assembling block co-polymer and magnetically active nanoparticles produced composite films with significantly enhanced magneto-optic response, and has been shown to lead to a new class of materials for magneto-optic applications. Through measurement of Faraday rotation and surface structure, an optimized family of PS-b-P2VP and FePt nanoparticles composites have been identified. A saturation effect with increased nanoparticle loading was identified, and the structural indicators of this behavior were investigated and described. It was found that cer-

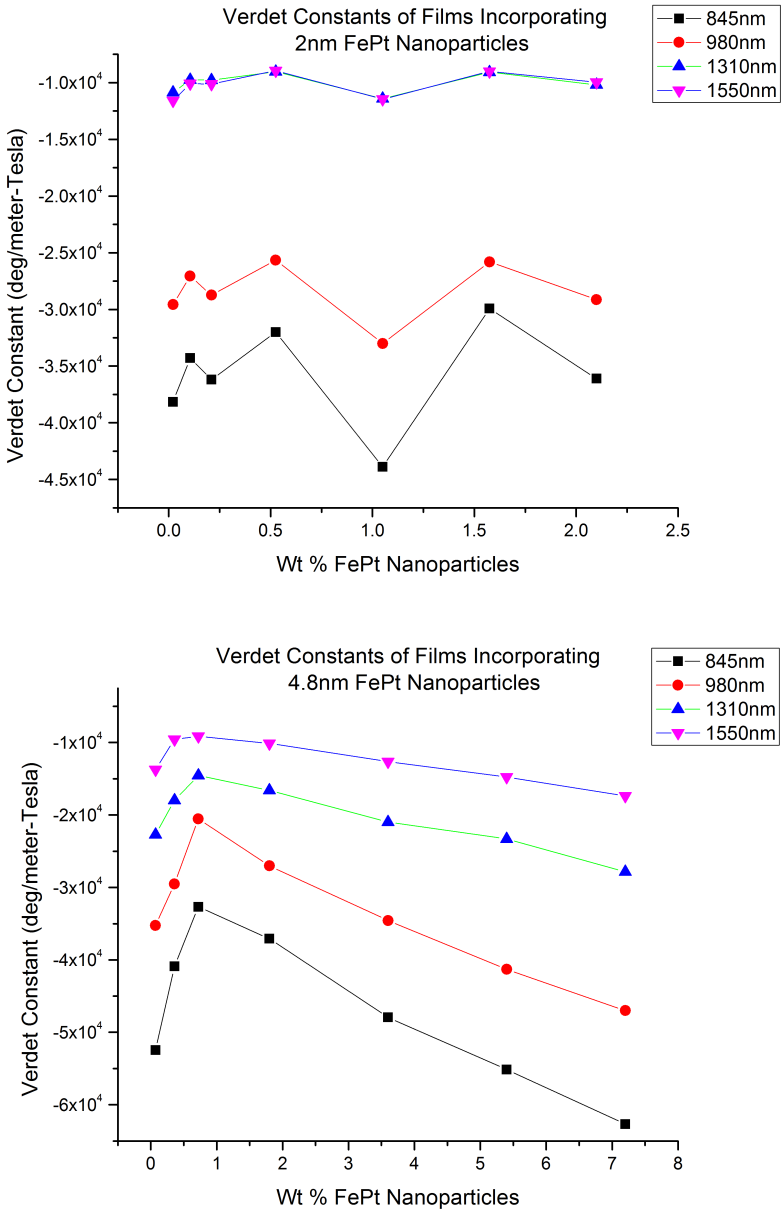

Figure 3.6: Measured Verdet constants plotted for two smaller particle sizes.

tain configurations produced performance exceeding that of commercially dominant magneto-optic materials.

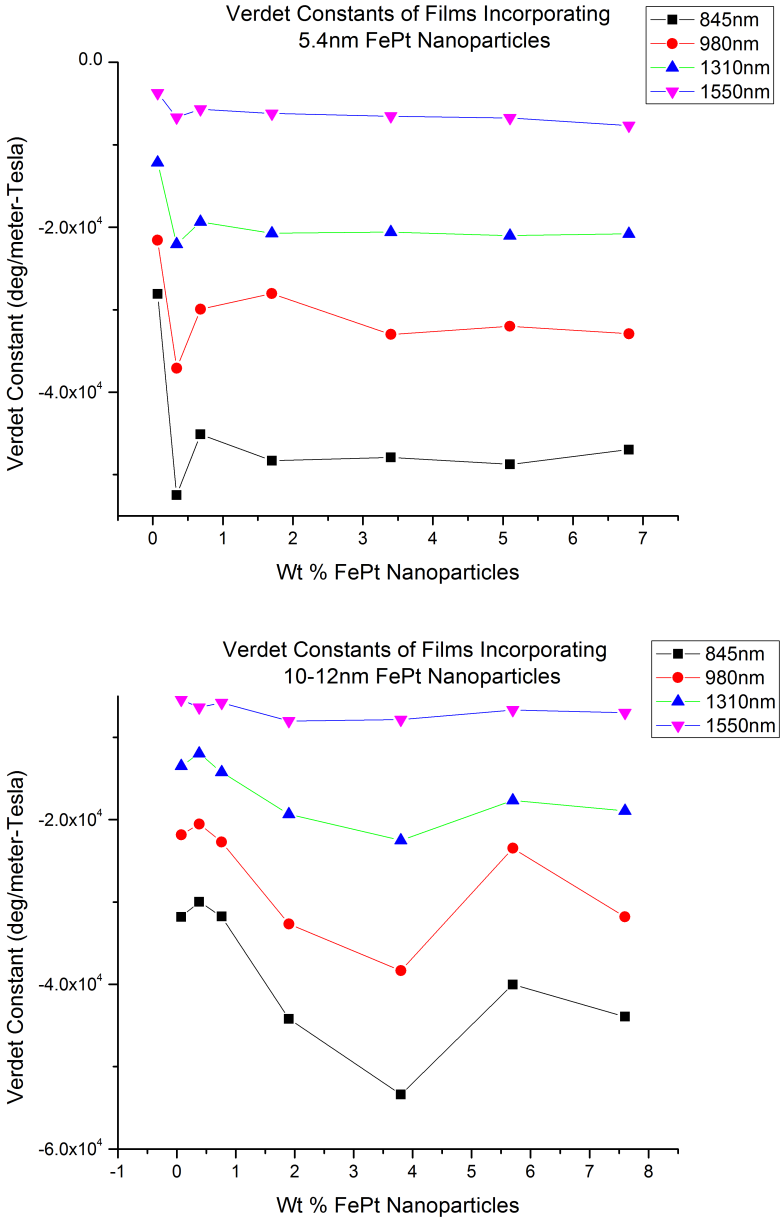

Figure 3.7: Measured Verdet constants plotted for two larger particle sizes.

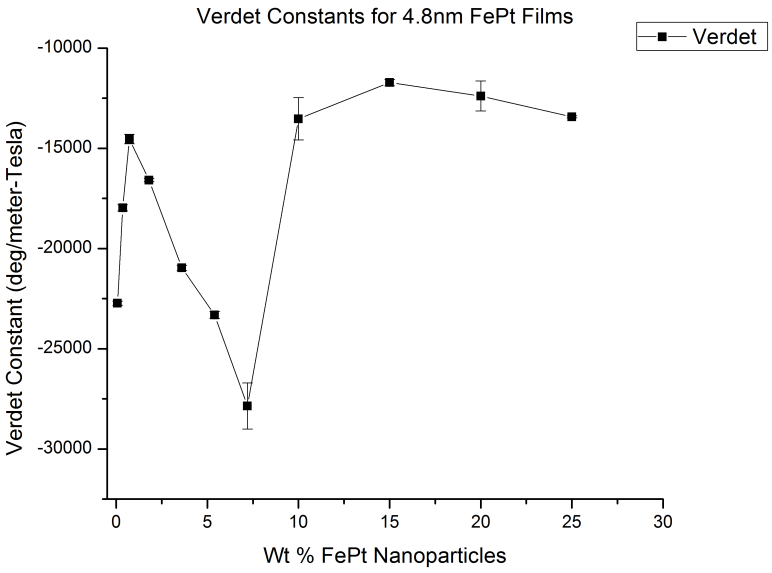

Figure 3.8: Measured Verdet constants over an extended range of particle loadings.

CHAPTER 4

7 x 7 DMD-Based Holographic Fiber Switch at 1550nm

4.1 Background

The first hybrid we'll be addressing is a combination of fiber optic telecommunications and active free-space holography. Optical fiber provides the long-distance and high-speed transmission medium for the bulk of the telecommunications traffic on earth. As such, advances in optical fiber networks provide direct and immediate benefit to both the network providers as well as the end users. Initially adopted due to the high speed of transmission and low signal attenuation over long distances, the advent of devices enabling amplification, switching, routing, and other traffic control operations in the optical domain were required before widespread installation could occur. While many advances have been made in the optical fiber itself, such as large-effective area fiber (LEAF) [40] and dispersion compensating fiber (DCF) [13], it is improvement in optical domain devices that will allow existing networks to better cope with the explosive growth of network traffic.

As shown in Figure 4.1, optical fiber connections exist on almost every level of networking. From a network-design vantage point, all this hardware exists as part of the physical layer, the lowest layer in the OSI telecommunications model [35]. The physical layer consists of hubs, repeaters, physical adapters; and it is in this layer that we find the actual devices and media associated with long-haul telecommunications. Chief among these devices is one capable of dynamically switching traffic, adding channels, and dropping channels, often referred to by the acronym ROADM (reconfigureable optical add-drop multiplexer). Many approaches exist to realize such a device, but the oldest and simplest is to use

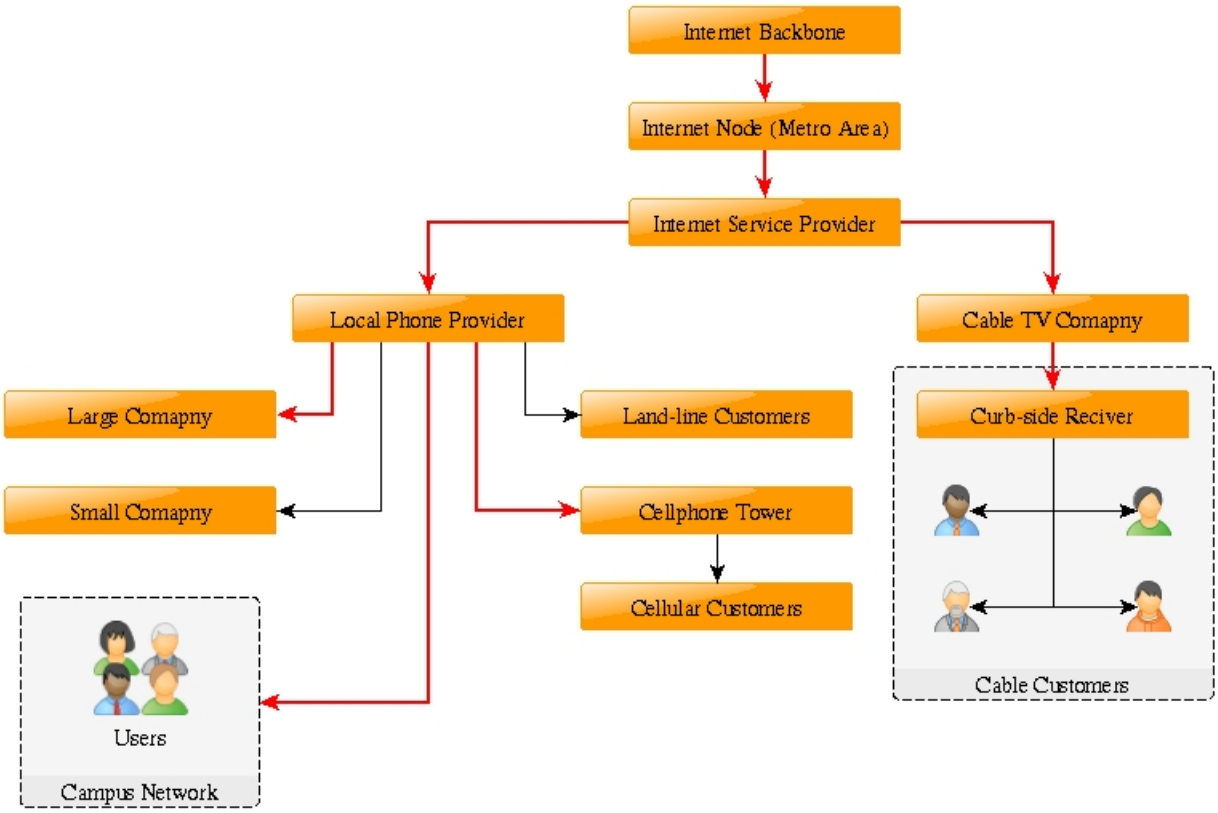

Figure 4.1: A schematic view of a local network based upon the illustration from Hecht's "Understanding Fiber Optics"[28]. Links shown with bold red lines utilize optical fiber.

an optical-electrical-optical ROADM. Often called an OEO, this device receives the optical signal and intelligently re-transmits that signal on the appropriate output. Before the invention of the erbium-doped fiber amplifier, OEOs were primarily used to regenerate optical signals being transmitted over large distances. Perhaps setting a trend, OEOs were quickly out-classed and out-priced by the purely optical amplifiers in the late 1980s [45], which, in conjunction with dense wavelength-division multiplexing [4] primed an explosion of development and deployment that started in the mid-1990s and lasted almost a decade.

Moving to the optical domain for switching and channel manipulations has

distinct benefits. Typically cost and energy are the primary motivation, as signal conversion into and out of the electrical domain is often expensive both in dollars and watts. Electrical domain operations are almost universally sensitive to the bit-rate and coding scheme of the optical signal being detected, but optical domain devices, once configured as essentially transparent, have no such restrictions. While the term "future-proof" gets used, it might be more accurate to describe the devices as "protocol and bit-rate agnostic", or perhaps "architecture insensitive". While there are distinct benefits to effecting ROADM operations in the optical domain, there does remain the caveat of packet switching. Only in the electrical domain can individual packets be discriminated and acted upon accordingly. While packet switching requires more expensive high-speed electronics, it is the one area that optical domain devices are not likely to soon make inroads.

Among purely optical domain ROADMs there are numerous strategies ranging from simply chaining of one-by-two switches (often utilizing the electro-optic effect) to effect a one-by-N switch, to using free-space beam-steering optics to re-couple light into desired outputs. Existing approaches have drawbacks, some are highly polarization sensitive, others have limited port-counts, and all struggle with insertion loss. In the following sections we describe the design, implementation, and characterization of a new sort of optical domain ROADM. By hybridizing the traffic-carrying optical fiber with a free-space hologram with a short reconfiguration time, we were able to address many of the drawbacks of existing devices while retaining the benefits of an optical domain device.

4.2 Introduction

The demands that bandwidth-intensive communication, entertainment, and storage are placing on existing data centers and optical networks are increasing exponentially. This growth continues to accelerate, with Cisco predicting annual global data center IP traffic to reach 7.7 zettabytes by the end of 2017 [11].

To minimize bottlenecks in information flow or data routing, the networks that handle this traffic rely on algorithms to continuously provision and allocate available bandwidth to where it is most needed. Further optimization of traffic is often limited by switching speeds and "loss of light time" caused by channel reallocation. The reconfiguration speeds of commercially available optical switches with large port counts are not yet sufficient for cross-connect and routing operations [49]. A smaller reconfiguration time leads to less time spent non-transmitting, making it a primary requirement of emerging switch technologies. Increasingly utilized hybrid architectures for modular datacenters, in which both electrical and optical switching technologies are used together, specifically highlight the need for fast optical domain switches [19].

Commercial 3D micro-electro-mechanical systems (MEMS) optical switches achieve switching by analog gimbaled movement of micromirrors to steer beams between outputs. One commercially available switch, based upon a 3D MEMS configuration, attains 25 ms switching time with an insertion loss of 2.0 dB across 320×320 ports [59]. This switching time is constrained by the analog nature of the switching, which relies on a feedback loop to settle the mirror at the position of best coupling. While this approach yields a very low insertion loss, this configuration is susceptible to port loss due to mirror or electronic damage that renders a given mirror inoperable.

An alternative approach is to use a liquid crystal on silicon (LCoS) spatial light modulator (SLM) as a dynamic diffractive element. The LCoS can modulate the refractive index across its aperture, providing a phase hologram for guiding. One implementation of this idea produced a 1×14 switch with insertion losses as low as 9 dB with switching times in the tenths of milliseconds [23]. A multi-mode ribbon fiber design recently described uses a custom molecule-based phase LCoS SLM, with 6×6 ports and 1 µs switching time, with a loss of 20.5 dB, and large

polarization sensitivity. A large portion of this loss, 11.5 dB, cannot be reduced as it originates in the polarizer/SLM design [12].

Optical domain circuit switches such as those mentioned provide distinct benefits over hybrid switches that operate across both electrical and optical domains. These switches are protocol and bit-rate agnostic and free-space diffractive switches, such as the one we have implemented, are scalable to larger numbers of ports and amenable to modular implementations without the same linear increase in power consumption. These properties drove our choice of core technology when designing the switch.

A digital micromirror device (DMD) provides an array of micromirrors capable of being switched between two angular orientations. A DMD based solution could fulfill requirements for speed, loss, and port count with fewer custom-made parts than competing designs. In addition, a holographic element-based switch can tolerate many mirror failures before dropping a channel, for example yielding losses of only 0.25 dB with failure of 2.5% of all micromirrors [41]. This resilience translates into a long device service life and architecture-independent operation, further distinguishing it from existing technology.

In one of our publications [41], we illustrated the feasibility of using these bulk manufactured components for free space beam steering, and demonstrated a visible light proof-of-concept device without fiber coupling. More recently, we have designed and implemented an innovative single mode fiber-coupled 7×7 port optical switch using a DMD as a holographic element. In addition we have further explored the system losses and possible mitigation strategies. The switch was characterized in terms of insertion loss, cross-talk, and polarization dependent loss, and was successfully tested in a network simulator.

4.3 Design

4.3.1 Concept

The design of this switch is based upon our initial proof-of-concept modeling and visible-light implementation [41]. The new system performs at telecom wavelengths in the C-band (1530 nm to 1565 nm) with coupling into and out of the system performed via single mode fiber. The switch utilized 7 single mode fiber inputs that can be independently switched to any or several of 7 single mode fiber outputs.

As shown in Figure 4.2, each input fiber has a 4 mm diameter collimation lens, L1. The collimated light from each fiber is incident upon a unique sub-region of the DMD surface, shown in black in Figure 4.3. Each of these regions display pre-calculated holographic patterns that diffract the light toward any given set of output fibers in the 1 cm^2 addressable area. A 48mm diameter anti-reflection coated lens, L2, maps the angular components of the diffracted beam into the focal plane where they are coupled into the output fibers. An example of an image sent to the DMD to guide Input 4 to Output 4 as well as the labeling scheme for the couplers are shown in Figure 4.3.

4.3.2 DMD

DMDs have been used in consumer projectors and rear-projection televisions for years, and as such there is an extensive body of data supporting their reliability and stability. Reliability studies have shown lifetimes of 10^{12} mirror cycles [16].

The DMD used in this implementation was a Texas Instruments DLP7000 with an array of 1024 $\times$ 768 micromirrors exhibiting a fill factor of 92%. The pixels are 13.68 µm square and correspond to a maximum diffraction angle of 3.25 deg by Bragg's law. By switching each mirror between two states, physically corresponding to tilting at $+12$ deg and -12 deg relative to the plane of the DMD,

we were able to realize the binary amplitude holograms necessary for switching. As previously measured, the DMD has a loss of light time of less than 12µs[20] and a total full-surface reconfiguration time including programming overhead and mirror settling of 43.5 µs [34], which as the sole active element determines the attainable switching speed. The size of the switching regions was dictated by the required grating resolution for effective fiber coupling, resulting in our choice of 7 inputs.

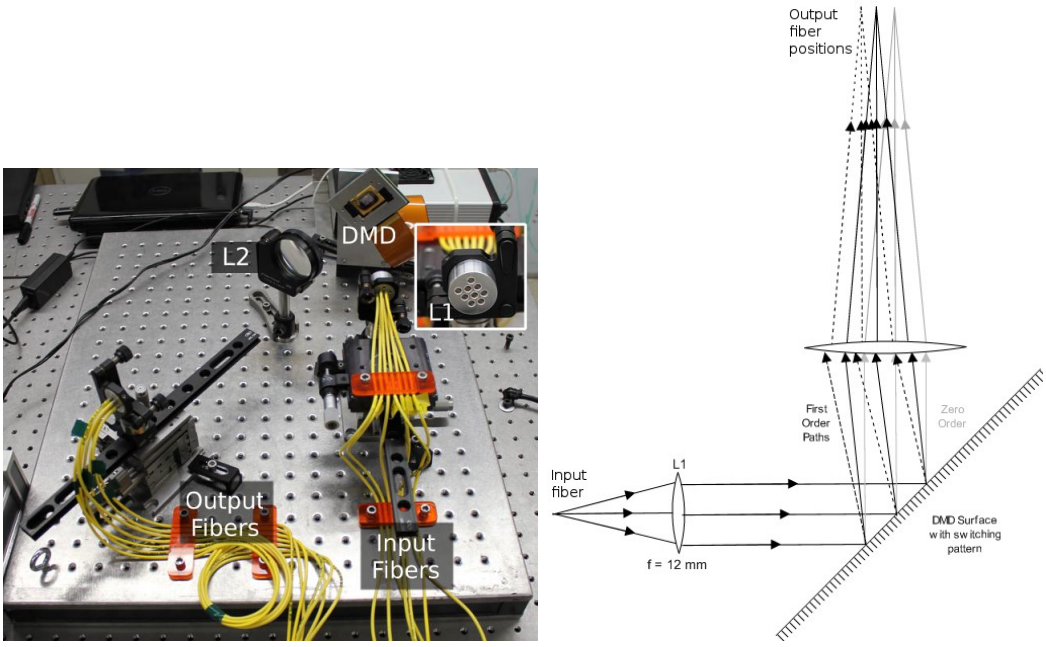

Figure 4.2: (Left) A photograph of the switch with the input bundle on the right. The inset shows the front face of the input bundle with the collimation lenses. (Right) An optical schematic illustrating the switching of a single channel. The guided beams are shown with solid black and dashed black lines. Angles have been exaggerated for clarity.

4.3.3 Hologram Design

The diffracted patterns resulting from transmission or reflection from a known structure have been calculated using scalar diffraction theory. The required holograms for ideal switching (i.e., one or more two-dimensional Dirac delta functions containing non-zero amplitude at all frequencies) contain an infinite number of

frequencies, each with specific amplitude and phase [26]. However, the DMD can only produce two amplitudes, a single phase, and a finite set of frequencies, meaning that the phase information must be discarded, the amplitude information converted to binary values, and the frequency information approximated by the realizable spatial frequencies (limited by the mirror size) of the DMD surface. This process of approximation was done using the Gershberg-Saxton iterative Fourier transform wherein discrete Fourier transforms are cyclically calculated and then inverted to minimize crosstalk between the output channels [21][54]. In situations where necessary spatial frequencies cannot be perfectly approximated, loss and crosstalk can result from light diffracted into unintended directions.

The implementation of a binary amplitude hologram results in multiple copies (± 1, ± 2, etc) of any desired image to appear in the image plane located symmetrically about the zero order. To maximize the transmission, the hologram is optimized to direct power into the +1 order that maps to a square region in the image plane inside which the output fibers must be placed. To minimize crosstalk we positioned the fibers such that unwanted modes fall in the space between the fibers [12]. As there are other orders present, a binary hologram can only realize maximum diffraction efficiency into the first order of 10.1% [36].

Component or Action	Loss (dB)
L1, reflection	< 0.01
DMD, reflection	< 0.01
DMD, diffraction eff.	10.6
L2, reflection	< 0.01
DMD, PDL	<0.14
SMF-28	
... Angular offset	<2.86
... Mode mismatch	3.80
Total fiber coupling	6.66
Total loss	**$<$17.43**

Table 4.1: Calculated loss budget for our implementation. This break-out is further discussed in section 4.5.1.

The DMD used has a fill factor of 92%, so 8% of the light is immediately absorbed by the non-reflective back plane of the DLP7000. The gaps between the mirrors produce a two-dimensional comb function in intensity that adds frequency components to the hologram along both DMD axes at the maximum realizable frequency. The high spatial frequencies mean that this light is diffracted far outside the region of the image plane accessed by the fibers. The combination of edge diffraction and inter-mirror absorption scales the efficiency by the square of the fill factor [68]. The combination of the diffraction efficiency and the fill-factor losses reduces the diffraction into the first order to ∼8.6% (10.6 dB). We discuss the mitigation of system loss in Section 4.5.1.

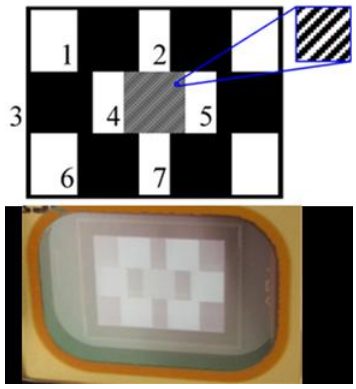

Figure 4.3: (Top) An example of an image, inverted for clarity, sent to the DMD to switch a single input with the channels labeled, the detail shows the periodic nature of the pattern. Here white and black pixels correspond to the two mirror states. (Bottom) A photograph of that pattern displayed on the DMD.

4.4 Experimental

4.4.1 Testbed Insertion at 1550nm

We implemented a single-mode fiber coupled 7×7 switch and demonstrated its ability to operate over the entire C-band. All the components are commercially available except for the fiber bundle housings (machined aluminum with slots

for the fibers and collimating lenses). The assembled switch was inserted into a networking testbed assembled in support of the Center for Integrated Access Networks (CIAN), a National Science Foundation (NSF) Engineering Research Center (ERC), provided an environment in which to simulate network traffic and test the data routing functionality of the switch. A Fujitsu Flashwave 9500 PS Packet Optical Networking Platform was used to provide the data traffic, which was sent through the switch and received by a second Flashwave node. We successfully transmitted an HD video stream through each switched channel without packet loss.

4.4.2 Experimental Results

The insertion loss was determined by measuring the optical power coupled into the input fiber and the power emerging from the selected output fiber. The crosstalk was similarly determined by measuring the sum of power coupled into all the other fibers. The polarization dependent loss was measured by rotating a half-wave plate in the beam path and monitoring the diffracted signal level.

The insertion loss was measured for each one-to-one switching configuration. The insertion loss varied between a minimum of 16.5 dB at zero angular offset and a maximum of 18.9 dB at the edge, where the angular offset was greatest (the case of an input fiber at one edge being routed to an output at the opposite edge). The measured diffraction efficiency of the DMD was 8.6%, matching the theoretical predictions. We found the crosstalk was below the detection limit, which sets an upper bound on the crosstalk (to and from any channel) of -70 dB. A breakdown of the sources of loss is presented in Table 4.1. The polarization dependent loss (PDL), shown in Figure 4.4, was measured to be less than 0.14 dB with a resolution of 0.05 dB. In this implementation, the switch was also highly wavelength-selective due to the spatial sensitivity of the coupling paired with the dispersive nature of the hologram. An increase in the loss of 3.73 dB per nm was found when departing from the design wavelength. Note that the holographic pattern can be adjusted to

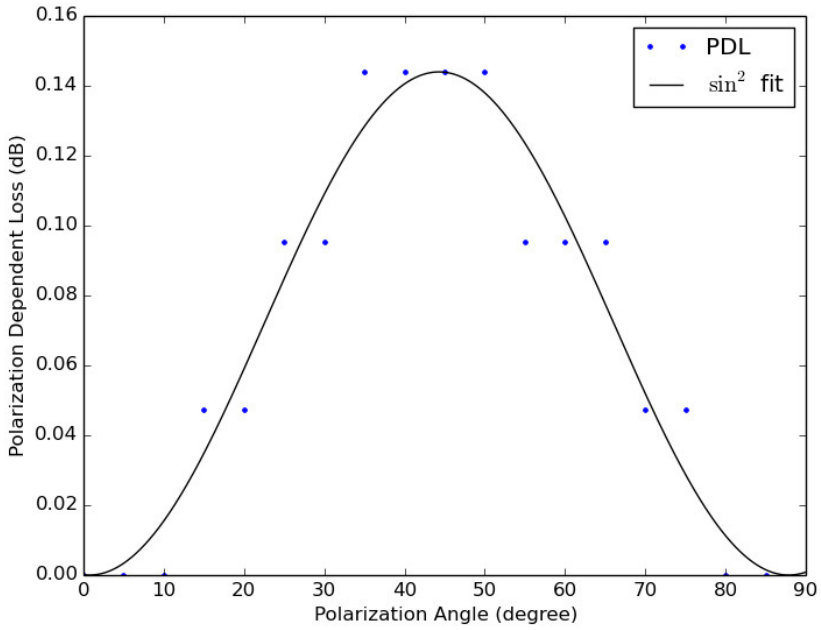

Figure 4.4: Measured polarization dependent loss data points and a sine-squared fit.

minimize loss at any design wavelength by recalculation.

4.5 Discussion

4.5.1 Loss mitigation and colorless operation

The majority of the losses can be mitigated in the following implementations. As illustrated in the loss budget in Table 4.1, the DMD losses are the highest priority. An alternative diffractive element, a piston-MEMS device, wherein the micromirrors move perpendicular to the surface by fractions of a wavelength rather than tilting relative to the plane of the DMD, has the potential to reduce insertion loss by ∼10 dB. A piston-MEMS device could generate a phase hologram, providing an alternative with diffraction efficiency into the first order of $> 80\%$ (0.96 dB) with as few as four available phases needed [67]. Piston-MEMs devices

with comparable pixel pitch, switching times, and fill factors are technologically possible [25]. Unfortunately, piston-MEMS devices lack the ubiquity of DMDs and do not presently enjoy the same economies of scale. The next largest contribution to the loss comes from coupling the light into and from the fiber arrays.

We can predict the coupling efficiency arising from mode-size mismatch (C_m), transverse offset (C_t), and angular misalignment (C_θ), normalized to unity [46] utilizing (4.1) and (4.2) below, which constitute a Gaussian approximation to the mode shape, wherein a is the diameter of the fiber core, σ is the full diameter of the beam (twice the beam waist), σ_0 is the initial beam diameter, f is the focal length of the lens, n_0 is the refractive index of the medium between the lens and the fiber, and d is the lateral offset. The full-diameter of the beam is given by the Gaussian beam relation below where z_R is the Rayleigh range of the beam. These can be optimized by selecting the correct optics for L1 and L2, the specifics of which are discussed in the following section.

$$C_m = \left(\frac{2a\sigma}{a^2+\sigma^2}\right), \quad C_t = e^{-d/(a^2+\sigma^2)}, \quad C_\theta = e^{-\theta/\theta_0} \tag{4.1}$$

$$\theta_0 = \frac{a\lambda\sqrt{a^2+\sigma^2}}{\pi n_0 a\sigma}, \quad \sigma = \frac{2\lambda f}{\pi\sigma_0}\left(1+\frac{f^2}{z_R^2}\right)^{-1/2} \tag{4.2}$$

It was found that aberrations caused by the collimating optic, L1, can cause as much as 6 dB loss depending on the combination of aberrations present [64]. This was addressed by employing a coated aspheric lens in that position, with parameters optimized for fiber coupling.

The wavelength dependence is another consideration for later designs. The switch presently acts as a narrowband wavelength filter, so a signal containing multiple wavelengths drops all but one when passing through the switch. One way to address this concern would be to break out the channels using an arrayed waveguide grating (AWG) before the switch and simply guide them along different

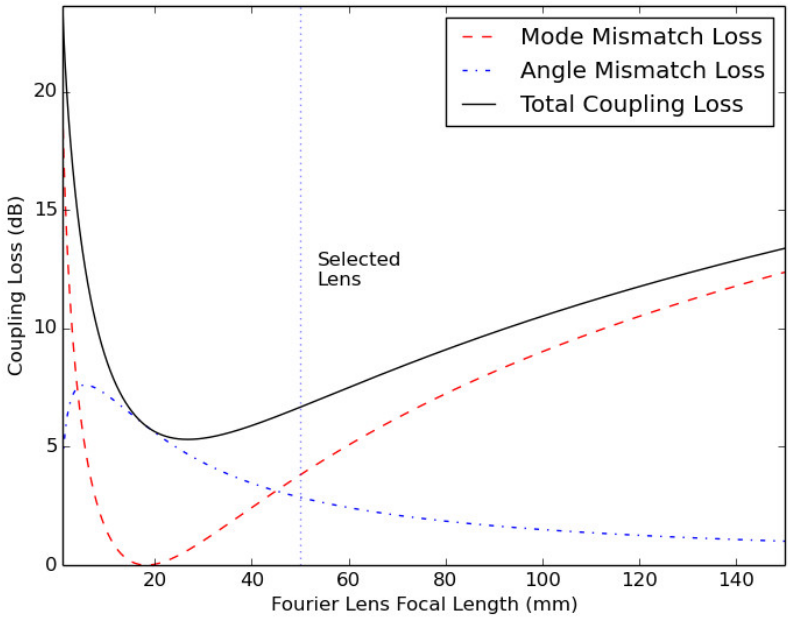

Figure 4.5: Mode size mismatch loss and angular mismatch loss for a range of lens focal lengths, calculated for our system parameters.

inputs, allowing each channel to be switched independently. This would realize a wavelength-selective switch (WSS), a key component in advanced optical networking. A second approach, illustrated in Figure 4.6, would be to use a second DMD or piston-MEMs device to remove the wavelength-dispersive angular deviation on the beams guided by the first DMD. Such a design would also inherently minimize the angular offset coupling losses across the entire output plane by ensuring that every guided beam will be within the acceptance angle of the desired output fiber. This approach, if employed in conjunction with the aforementioned piston-MEMs devices, would address the fiber coupling without introducing additional loss.

4.5.2 Lens Selection - Optimizing Coupling

(4.1) and (4.2) can be used to guide selection of the lens, L2. First we can determine the beam waist at all points in the system using Gaussian beam imaging and

propagation. The beam waist (radius) of the Gaussian that exits the fiber into free space is 5.25 µm [37], and the 12 mm focal length collimation lens yields a waist of 1.13 mm. Coupling into fiber after the lens presented two competing issues: the mode-size mismatch between the focused beam waist and the fiber core, and the angular offset between the direction of propagation and the fiber axis as illustrated in Figure 4.5.

At shorter focal lengths, the loss is dominated by angular mismatch, and at long focal lengths the loss is dominated by mode-size mismatch. We selected a 50 mm focal length lens for this iteration as it provided the correct magnification for our couplers and sufficient performance for a proof of concept. In principal, the coupling loss can be further reduced to 5.3dB.

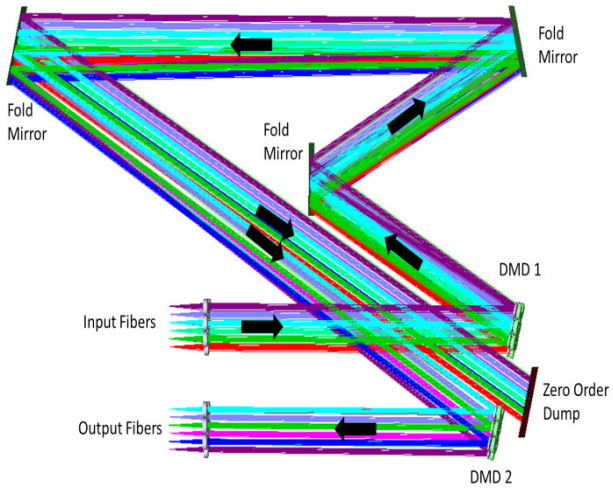

Figure 4.6: A schematic layout for an implementation utilizing two DMDs or piston-MEMs devices to mitigate wavelength dependence and angular coupling losses.

4.5.3 Scalability - Extending to Larger Port Counts

Large port counts are a desirable feature for a practical optical switch as this reduces the total component count for a given network capacity. The number of input ports is limited by the number of pixels on the DMD, as each must have the same total number within their footprint on the DMD surface to achieve the same switching efficiency. The regions reserved for each beam footprint are illustrated in Figure 4.3. The output port count is limited only by the spatial frequencies the DMD can generate, and in general is much larger than the input port count for a single DMD. Using a device with a larger pixel count and/or smaller pixels, or tiling existing DMDs, directly scales the number of input ports. By moving to more densely packed output planes, containing fiber ribbons or arrays, the output port count can be increased without changing the maximum angular deviation and angular offset loss. Further details regarding the port-count scaling of a DMD-based switch are included in a published work [41] where we illustrate that a 30 $\times$ 30 switch is possible using the Texas Instruments 0.95 DLP, and 144 $\times$ 144 port count using a commercially available 4K DMD [59].

4.6 Conclusion

We have designed and implemented a free space 7 $\times$ 7 C-band non-blocking switch using a DMD as a holographic element, with a potential full reconfiguration time of less than 43.5 µs. The switch enables high reliability full optical cross-connect and wavelength-selective switching capabilities and the possibility of modular configurations for very large port counts. This was done with commercially available optics. This DMD-based proof-of-concept provides a basis for further work with a low-loss piston-MEMs device. Moving from an amplitude hologram to a phase hologram will reduce the diffraction losses by almost 10 dB without additional changes to the design. The two-pass configuration enabled by piston-MEMs permits the mitigation of wavelength dependence and angular coupling losses. The fundamen-

tal design shows clear potential for applications in optical networks and data centers.

CHAPTER 5

Hybrid Solar Collector

5.1 Background

Our experiences with holography proved valuable beyond the world of photonic and display devices. A hologram can be thought of as a spatial variation in the refractive index and absorption across some clear aperture, used to shape the intensity and phase of a wavefront. If this concept is extended down the z axis, it would describe a volume hologram. In such a volume hologram, if the profile does not vary in the transverse directions, x and y, what we're describing is called an interference filter. Very much in the same wheelhouse as Fabry-Perot etalons and fiber Bragg gratings, well designed interference filters can exert incredibly fine control over spectral features of light passing through or reflected from them. In practice these filters are produced by depositing layers of dielectric materials (and occasionally metals) in a stack on an optical surface. These layers are generally on the order of tens to hundreds of nanometers thick, fractions of a wavelength, providing them with their common designation, thin film filters. Given the spectral selectivity and performance possible with these filters, paired with their stability, environmental resistance, and availability, they proved to be the right glue to join two existing technologies that each balanced the weaknesses of the other.

Combining two complete utility-scale solar energy collection technologies was the largest and most complete hybrid our work addressed. The prevalence of solar energy, both in the public dialogue and the scientific world, has been rapidly increasing over the past ten years, as evidenced by increased investment in all sectors [43]. While numerous factors (e.g. energy independence, remote distribution) have spurred research into solar energy, developments in climate research over the past

decade have provided the sense of urgency needed, and public support for, more widespread adoption of solar.

Each solar technology possesses specific drawbacks, but the general issue is simply not being competitive on a dollars-per-watt basis with existing conventional power generation methods. This issue is common to almost all renewable energy sources, primarily due to the presently low price of coal and natural gas, but the balance is shifting. 2013 was the first year on record to see larger increases in capacity among renewable energy sources than non-renewable ones, and in 2014 renewables accounted for 60% of the newly installed capacity [43]. A breakout of the major categories of renewable sources is given in Table 5.1. While subsidies and public pressure can force progress, improved efficiency is necessary for practical long-term usage.

	Capacity (GW)		
Technology	2004	2012	2013
Hydropower	715	960	1,000
Bio-power	<36	83	88
Geothermal	8.9	11.5	12
Solar PV	2.6	100	139
Solar CSP	0.4	2.5	3.4
Wind power	48	283	318

Table 5.1: Progress in Renewable Energy Generation Capacity [43]

The single most common solar collection technology is the photovoltaic cell, used both at the consumer level in rooftop solar panels and the utility scale in solar farm installations. In these cells an absorbed photon generates a carrier-pair, which can be extracted as electrical current, very much like a light-emitting diode operated in reverse. Various innovations in the cell materials, design, and deployment have lead to significant improvements in the efficiency of these cells, however they suffer for want of better batteries. The power output of a PV plant during peak production can often outstrip demand, while nighttime energy consumption cannot

be harnessed without some way to store the power. Battery technology that does exist on the utility scale is prohibitively expensive and difficult to deploy. More direct physical schemes, such as pumping water to an elevated tank with the excess power have been attempted, but have proven mechanically failure-prone [1]. Countries with large installations of renewable sources have had to take numerous precautions to prevent rainy or overcast days, solar eclipses, and other conditions from unduly disrupting their power grids [44].

The solar thermal approach, wherein the light is collected as heat, adequately addresses the issue of storage. Heated water, oil, or molten salts, can be easily stored at elevated temperatures in a well-insulated tank, and this stored heat can be easily converted to electricity when energy is needed. Carnot efficiency, the limit on how efficiently this heat can be converted into useful power, is the real thorn in the side of solar thermal. While high-temperature installations can attain Carnot efficiencies as high as 50% [22], this is based upon the temperature of the collector compared to ambient. The temperatures at which heat is stored are lower and the "cool side" is often well above ambient, as such reported efficiencies range from 10% to 15%. At present these two approaches are not employed symmetrically, of the installed solar electricity generation capacity, 97.6% is PV while only 2.4% is CSP [50][6].

5.2 Introduction

Approaches to improve the efficiency of solar collectors by manipulating the spectrum of the incident light have been investigated for many years [17, 15, 52], and the concept of splitting the spectrum between photovoltaic and photo-thermal bands is a well-established one [32, 33]. Thin-film filters have been employed on their own or in conjunction with liquid absorbers to affect a band pass filter for individual single junction cells [15, 48], or as a method to split light between

multiple independent single-junction devices[63].

Multi-junction photovoltaic cells present the highest potential efficiencies [27], but introduce additional difficulties in the design of the system. Foremost amongst the difficulties are the necessity to balance the currents between the junctions in the device, and the concentrations at which they perform best. Dichroic filters are a potentially useful tool for combining a spectrum-selective system design with efficient multi-junction photovoltaic cells. However, the design of these filters is non-trivial, and depends on the properties of the junctions, the optical system geometry, and environmental factors at the installation site.

In this chapter we present a method we have developed for producing dichroic filter designs for hybrid systems with current-matched photovoltaics, as well as a design produced by this method for installation in Tucson, AZ.

5.3 Materials and Methods

Photovoltaic cells, as well as the individual junctions within multi-junction devices, possess different external quantum efficiencies (EQEs) at each wavelength. This typically takes the shape of a contiguous band, bound on the long wavelength side by the wavelength corresponding to the bandgap, and falling off more gradually on the short wavelength side. This is due to the fact that photons possessing insufficient energy to excite carriers across the bandgap cannot be absorbed, and photons with excess energy result in the generation of waste heat in the form of phonons. The larger the excess energy, the less efficient the conversion of photons into current, and the more waste heat is generated.

By cascading junctions in a single device one can achieve a wider band of high EQE and therefore higher efficiency over the whole input spectrum. A drawback, however, is that the current produced by the individual junctions must be matched

for efficient extraction [66]. Current in excess of the smallest current in a given junction is effectively lost.

Dichroic filters are a common tool for engineering the spectrum of light incident on photovoltaic cells. By limiting the band of incident wavelengths to the region with highest EQE, we can minimize the waste heat generated in the cells and even direct the unused wavelengths to a solar thermal receiver for dispatchable power generation. For a single junction a band pass filter is a tenable solution, and progress has been made on wide-angle filters of this type[31] but in a multi-junction system that must cope with a variety of angles of incidence, such a filter will provide mismatched junction currents under most conditions. Careful design of the shape of the filter function, paired with an understanding of the incident angles on the dichroic, can be used to current balance the junctions under the expected illumination conditions and angles.

The use of a dichroic filter for shaping the spectrum, rather than an absorbing liquid or solid, brings additional challenges. Changes in the incident angle of the light on the dichroic filter cause the spectral properties to change[42]. Generally this results in a blue-shift of the characteristic with increasing angle that goes approximately as the cosine squared of the angle[65]. The refinement process must simulate the coating performance under a sufficient number of angles of incidence to appropriately gauge the merit of a given design.

5.4 Theory and Calculation

The goals of a particular design are based upon the EQE of the junctions, the optical system surrounding the coating (if any), and the location of the installation. From these starting points we can obtain the necessary information to build a merit function that will serve as an appropriate target for refining the coating design. While the junction performance is directly considered during refinement,

the location provides the expected illumination spectrum and angular distribution of that illumination and the optical system determines the angles of incidence on the coating. This process is outlined schematically in Figure 5.1.

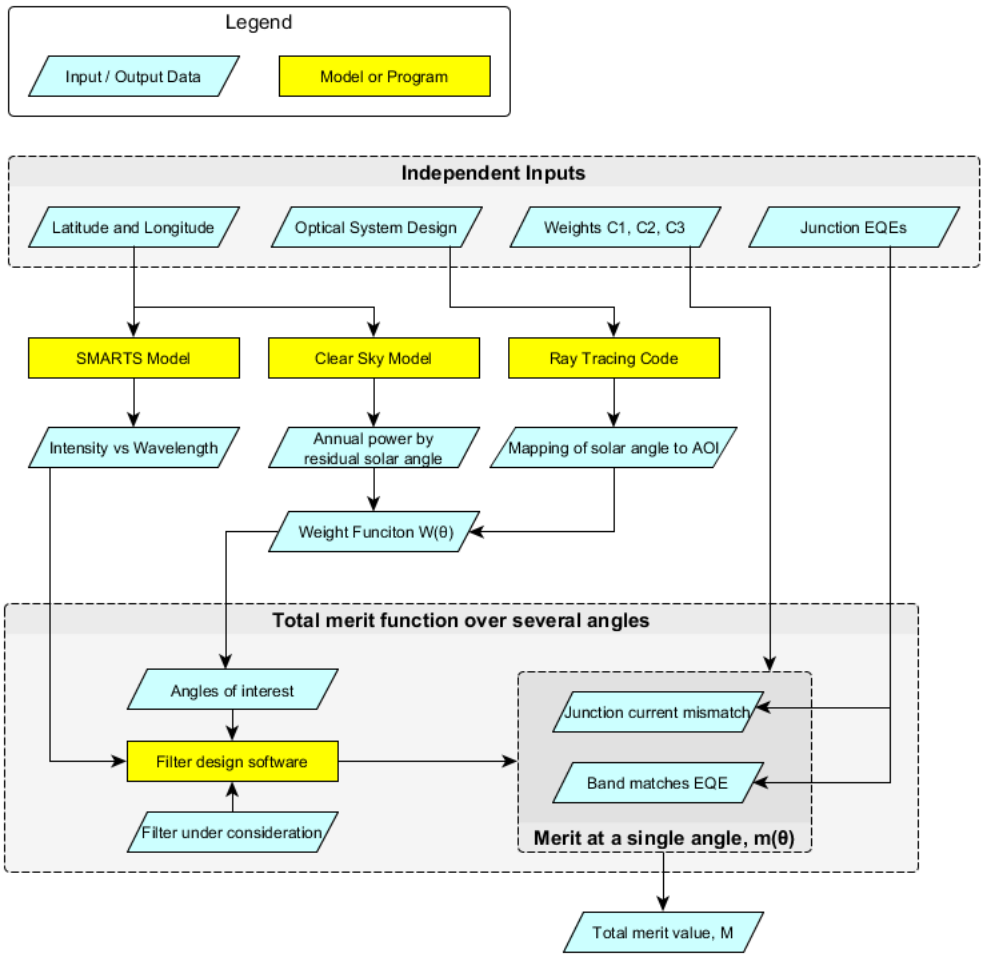

Figure 5.1: Workflow for merit function design

The goals of the dichroic mirror design can be thought of at two levels of priority, namely maintaining the current balance of the junctions and keeping the leakage (reflection in the transmission window and transmission in the reflection window) to a minimum. Together these ideas drive the design of the merit function.

In the merit function we break these concerns out into three pieces. We calculate the reflectance over the input spectrum and determine the average reflection in the transmission window ($\overline{R_T}$) and the average reflectance in the reflection window ($\overline{R_R}$). The bounds of these windows are based upon the EQE of the cells and the desired split between photovoltaic output and solar thermal collection. Within the band directed toward the photovoltaic cells we determine for each wavelength which junction the photons will be absorbed in and the photon density of the input spectrum. After iterating through each wavelength, the cell mismatch (Δ) can be calculated. Each of these quantities is given a weight, and the weighted sum provides the merit value. These parameters were chosen such that ($\overline{R_T}$), ($\overline{R_R}$), and Δ are all bounded by 0 and 1, so the maximum value that the merit function (m) can take on is the sum of the weights. The weights, c_1, c_2, and c_3, are chosen to reflect the relative importance of the final properties of the system.

$$m = c_1\overline{R_T} + c_2(1 - \overline{R_R}) + c_3\Delta \tag{5.1}$$

The coating will, in general, operate at more than one angle of incidence (AOI), so the relative prevalence of each AOI must be determined. This results in a weighting, $W(\theta)$, that provides the relative importance of performance at each AOI. The method we employed to determine this function is detailed in the following section. To find the total merit function of the system, merit values are calculated for a subset of angles and summed using the weights for each angle (Eq 5.2).

$$M = \sum_{n=1}^{N} W(\theta_n)m(\theta_n) \tag{5.2}$$

If the weightings and input spectrum are chosen appropriately, minimizing the value of this merit function using the refinement methods available in thin film design software will provide an optimal current-balanced design. This comes with the usual caveat of ensuring the refinement has produced a physically realizable design.

5.5 Case Study - Concentrating Hybrid Solar Collector

5.5.1 System Parameters and Materials

The system we worked with utilizes a dichroic mirror to split the solar spectrum. Wavelengths where multi-junction photovoltaic cells are most efficient are reflected toward the cells, and all other wavelengths are passed to a thermal receiver. Taken together, a higher total energy efficiency can be attained. Employing this approach simultaneously provides immediate power during the day from the PV and dispatchable power during the night from stored thermal energy. Based upon the site of the installation (Tucson, AZ), the available annualized solar energy and solar angles were determined. The AM1.5D spectrum was used for our dichroic refinement. This spectrum and the EQE curves for the two junctions of our multi-junction photovoltaic cells are shown in Figure 5.2.

Using dielectric thin film coatings in the context of a concentrating photovoltaic collector places practical restrictions on the materials used. To maximize efficiency, low absorption at all solar wavelengths is critical. The materials should also be selected to minimize residual stress that might lead to failure at the elevated temperatures encountered during normal operation. This selection process led us to select Ta_2O_5, Al_2O_3 and SiO_2 as our potential materials. These three materials provide high, intermediate, and low refractive indices necessary for a high performance coating while possessing low absorption over the band of interest as well as mechanical compatibility.

5.5.2 Angular Analysis, $W(\theta)$

In the system described, as the dichroic mirror is positioned after a primary concentrating optic, the distribution of incident angles expected must be calculated. The entire system tracks along a north-south axis, leaving a residual solar skew angle (θ_{skew}) between the direction of the sun and the optical axis of the system, as

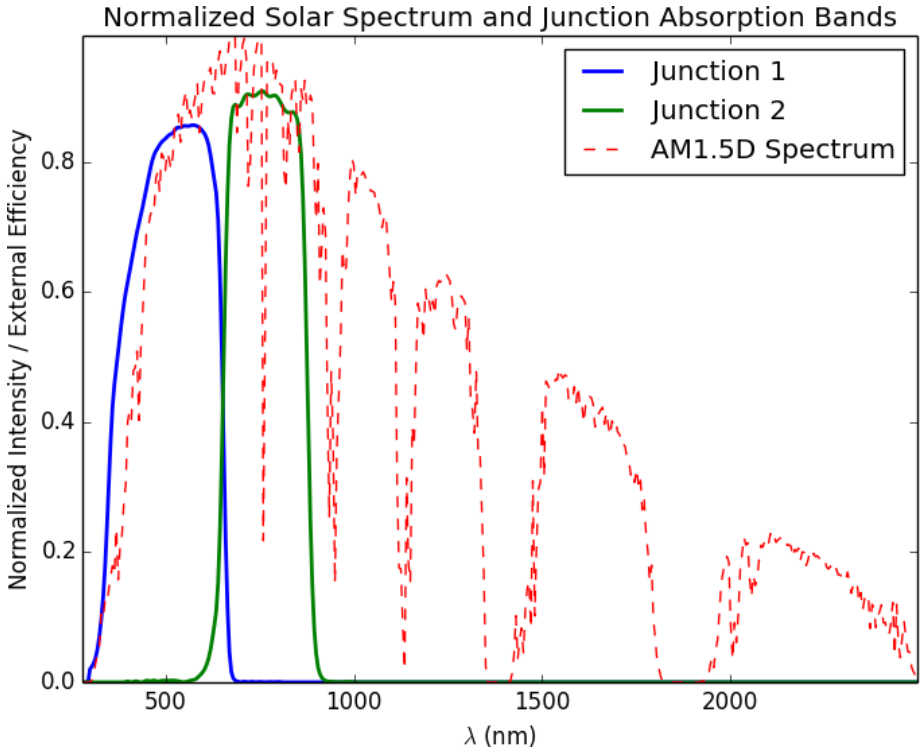

Figure 5.2: The AM1.5D solar spectrum and the external quantum efficiency (EQE) of the two photovoltaic junctions.

shown in Figure 5.3. The relative annualized energy at each solar skew angle was calculated using the simplified clear sky model[8] with parameters for Tucson, AZ. The way in which solar skew angles map to the AOI on the dichroic mirror (θ) was determined by tracing rays through our system in Zemax OpticStudio 14 for each combination of θ_{skew} and entrance pupil coordinate. Each of these distributions was weighted by the annualized relative energy at the corresponding skew angle, and the distributions were summed over all skew angles. The resulting curve, shown in Figure 5.4, provides the weighting function for the AOI on the dichroic mirror.

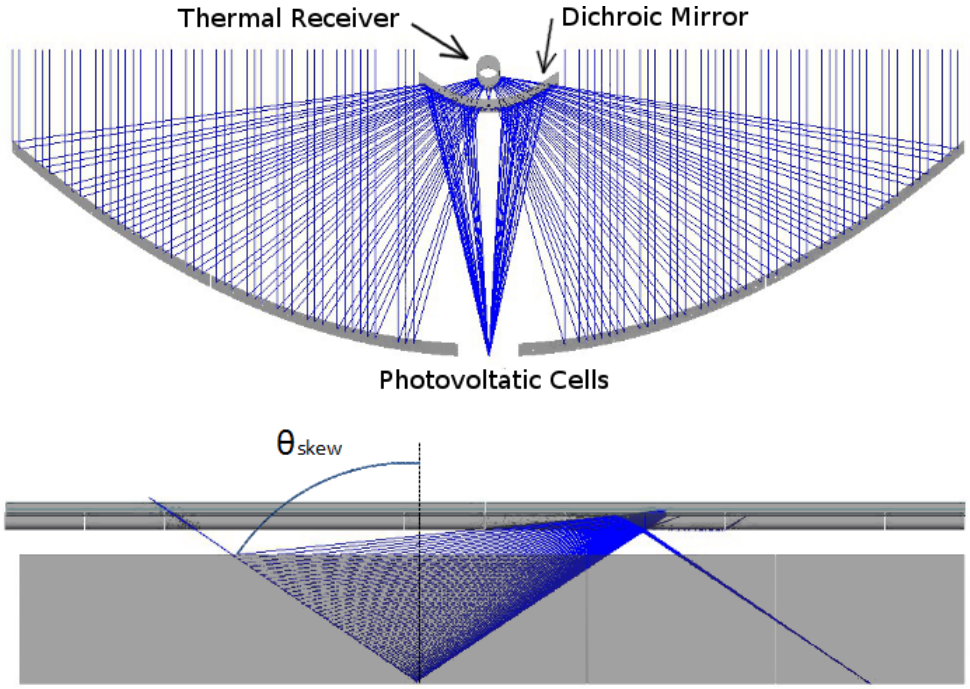

Figure 5.3: (Top) Schematic system parallel to tracking axis. (Bottom) System perpendicular to tracking axis with apparent solar skew angle.

5.5.3 Optimization and Resulting Performance

For our system the highest priority is ensuring that the photons in the transmission band reach the thermal pathway, as dispatchable power was weighted more strongly for our site. Due to this concern the transmission coefficient (c_1) is kept the largest. Within the reflection band, it is more important to keep the cells balanced than to

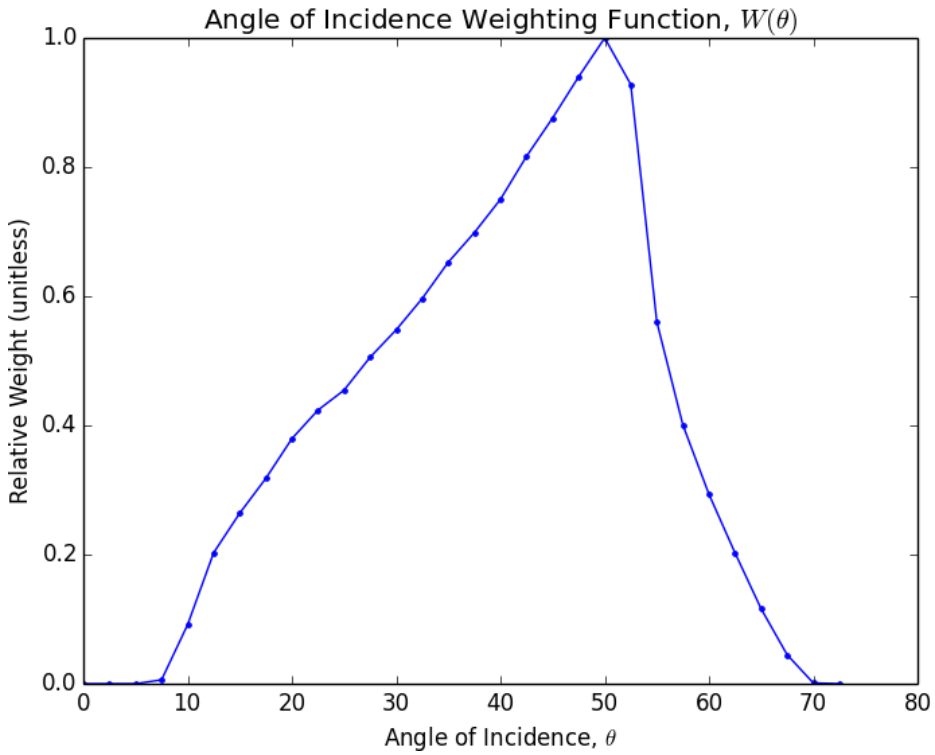

Figure 5.4: Weighting function $W(\theta)$, providing the prevalence of AOIs on coating throughout a full year in Tucson, AZ.

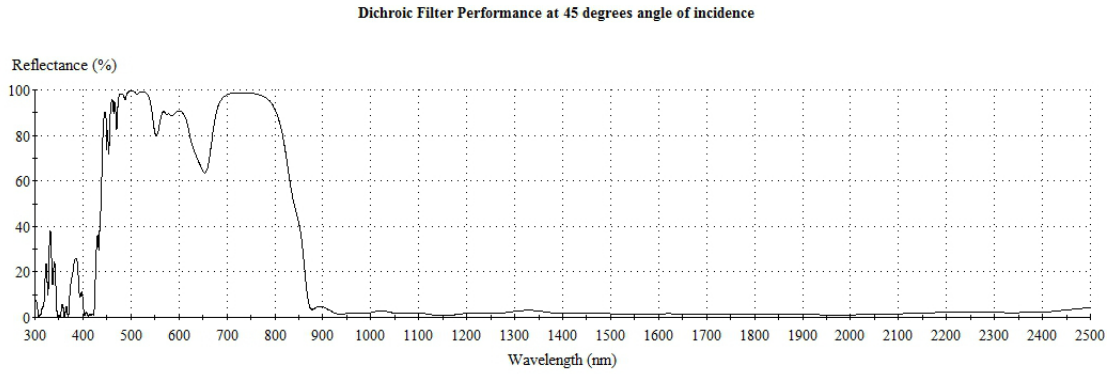

Figure 5.5: Performance of a current-matching filter at 45° AOI.

provide the highest level of reflection, therefore c_2 was kept smaller than c_3. This ensures that transmitted photons can still be captured as useful heat, while the loss due to current mismatch is mitigated.

As a starting point for refinement we chose a taper of SiO_2 and Ta_2O_5 where the layer optical thicknesses vary linearly between an eighth-wave to a quarter wave over 40 layers. This family of designs produces wide high-reflectance bands with reasonably low reflection outside those band. While a single quarter-wave stack, or combination of several stacks, generally provide similar properties, it was found that tapered designs converged more rapidly during refinement. The refinement was carried out in the Essential Macleod software package using a combination of the included simplex and optimac methods. The scripted merit function utilized is presented in it's entirely in Appendix C.

The result of the refinement was a 65 layer coating utilizing all three materials. The mean-polarization intensity reflectance spectrum of a refined design at 45° AOI is presented in Figure 5.5. The dip in reflectance around 650 nm was a common feature among all the well-balanced designs, with the depth and placement changing slightly as the weightings changed.

To characterize the performance of the design, the magnitude of the current mismatch was tabulated every degree inside the range of angles expected on the coating. The relative currents produced by the cells and percentage mismatch as functions of incident angle are shown in Figure 5.6. When the system is deployed, a bundle of incidence angles will be present under any given illumination; therefore the performance at a given solar skew angle will depend on the filter performance at a variety of incidence angles. Assuming uniform illumination of the entrance pupil, the distribution of incidence angles used to calculate the weighting curve (shown in Figure 5.4), along with filter performance at each incidence angle, can be used to determine the effective spectral reflectance as a function of solar skew angle. This

effective reflectance is plotted alongside the intensity reflectance at each incidence angle in Figure 5.7. Averaging the reflectance over the coating angles for each solar skew angle distribution has the effect of suppressing ringing in the infrared region and reducing the impact of the blue-shifting of the features with changing angle.

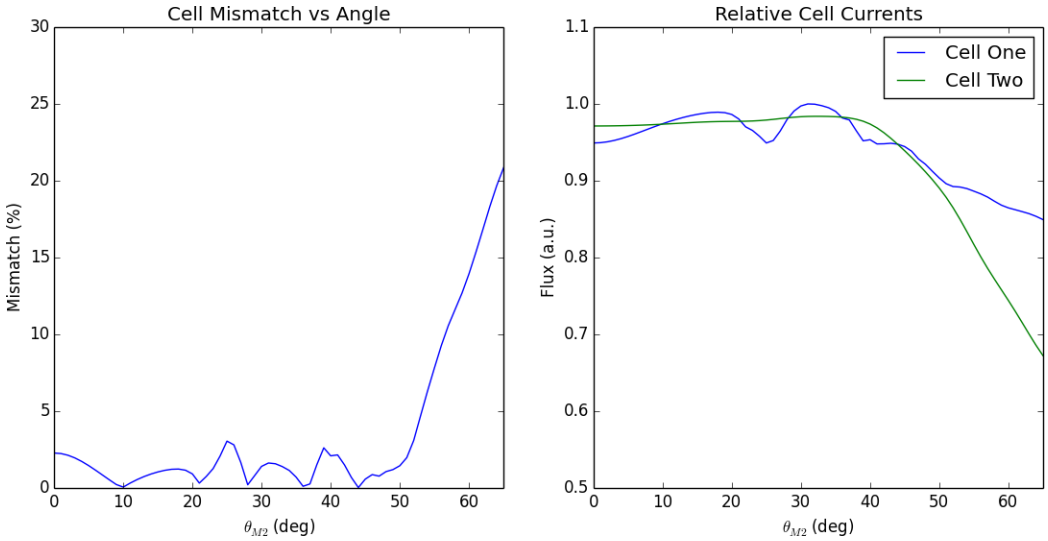

Figure 5.6: The relative current mismatch (left) and individual junction currents produced (right) as a function of incident angle.

The final coating design behavior was fed into a model that predicted the solar angle, spectrum, and intensity for each hour of sunlight for a year at the chosen installation site. Utilizing the mapping between exterior angle and incidence angle at the mirror, the filter behavior at each incidence angle, and the solar characteristics, we can determine the annualized performance of the system. For the concentrated photovoltaic branch, this model predicts an efficiency of 14.36%, normalized to the direct normal incidence.

5.6 Conclusion

An approach for designing a dichroic coating to maintain the current balance of multi-junction photovoltaic cells under a variety of illumination conditions has been outlined and demonstrated. A thin-film dichroic reflector for use in a concentrating

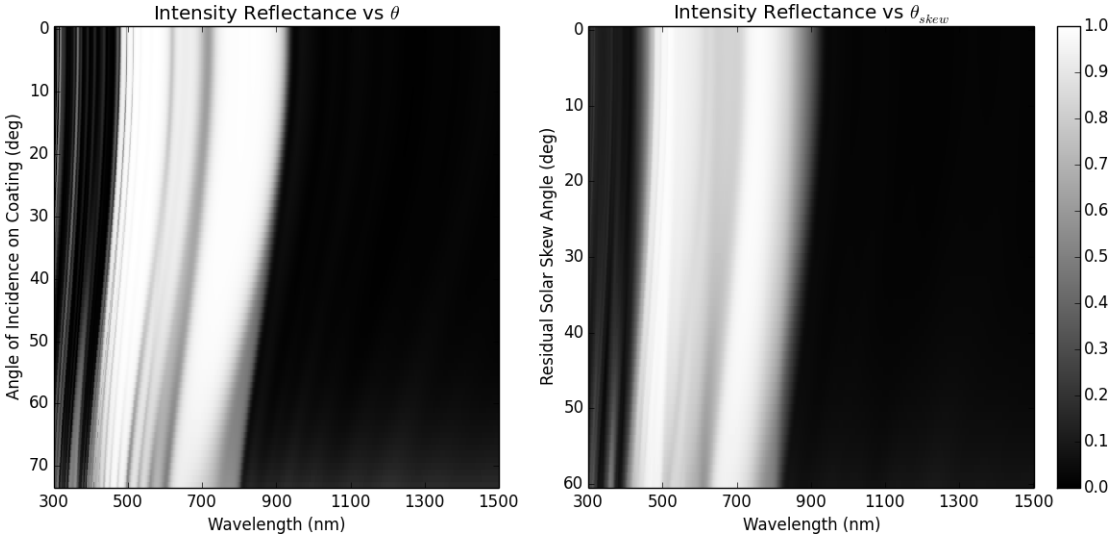

Figure 5.7: The intensity reflectance as a function of incidence angle (left) and residual solar skew angle (right).

hybrid solar collector produced using this method showed substantial improvement over a simple band-pass filter. This approach, in conjunction with the specific parameters of our site and requirements, has produced designs with a marked dip in reflectance that serves to maintain balanced current under varying illumination conditions.

Appendix A - Data Processing Script (Python)

```
# Magneto-optic Verdet Constant Measurement
# AC Measurement Post-Processing Script
# for Python 2.6
# Alex Miles - Originated 2/14/2015
#            - Last edit  3/17/2015

from numpy import array, linspace, mean
from pylab import *
from scipy import sin, loadtxt, stats
from Tkinter import Tk
from tkFileDialog import askopenfilename
from scipy.interpolate import interp1d

# Processed file output columns are...
# A, B,     C,  D,  E,       F
# V, Gauss, AC, DC, FRTotal, FR
# Where FR Total = -57.296*AC/(800*DC)

# Open the file with the measured data
Tk().withdraw()                     # we don't want a full GUI, so
                                    # prevent root window from appearing
fname = askopenfilename()           # show an "Open" dialog box and
                                    # return the file path
fname_root = fname.split('.dat')[0] # Find the root file name for
                                    # saving the processed version.

# This function is the empyrically determined map between drive voltage
# and magnetic field in Gauss.
```

```
def field_mapping(X):
  return X*1844.2697

# This function reads in the file. It takes arguments to print verbose
# statements (verb), set the wavelength, and to turn background correction
# on or off.
def read_in_data(fname, verb=False, wl="glass", background=True):
  print "Using substrate data at %s. MAKE SURE THAT'S RIGHT" % wl
  F = open(fname).read() # Open the file, read it into a string
  lines = F.split('\n')  # Split the string into a list, each element is one line
  list_of_measures = []  # Make an empty list for the measurments in the file

  # Make lists for : Description, Signal, Phase, AUX1
  desc, signal, phase, aux_one = [],[],[],[]
  # Make lists for : AUX3, Frequency, Voltage
  aux_three, freq, volt, gauss = [], [], [], []
  old_field = -1.0       # Store an impossible previous field to trigger the first set

  # Loop through all the lines in the file we read in, except the header, so [1:]
  for line in lines[1:]:
      if len(line) < 5: continue      # This allows the loop to ignore empty lines.
      bits = line.split(',')          # Break the line into component parts
      new_field = float( bits[6] )    # Store the new field value
      if (new_field != old_field) and (old_field != -1.0):
        # If the field has changed, add stored details to
        # the list of measures, make new empty ones, and
        # update the "old field"
        list_of_measures.append( [volt, gauss, signal, aux_three] )
        old_field = new_field
        if verb: print "Added data for field value %0.2f" % volt[-1]
        desc, signal, phase, aux_one = [], [], [], []
        aux_three, freq, volt, gauss = [], [], []
```

```
    # Regardless, update the field value and add the data from line to the lists

    old_field = new_field
    signal.append(float(bits[1]))
    phase.append(float(bits[2]))
    aux_one.append(float(bits[3]))
    aux_three.append(float(bits[4]))
    freq.append(float(bits[5]))
    volt.append(float( bits[6]))
    gauss.append(field_mapping(float( bits[6]))) # Convert drive voltage to Gauss

# It should always work, but just in case, we have an error notifier here.
# Any file corruption will trigger this
try:
  list_of_measures.append( [volt, gauss, signal, aux_three] )
  if verb: print "Added data for field value %0.2f" % d7[-1]
except:
  print "ERROR with line:"
  print line

# For brevity, we store the whole list as the variable "D". This is N x M x 25,
# where N is the number of voltage levels, M is 7, the number of stored values,
# and 25 is the number of measured values for each stored value.
D = list_of_measures


# We now step through the each voltage (a), and each measure (b), and replace
# that inner-most list of measurements with the average of those measurements.
# D is now N x M x 1.
print "Averaging..."
for a in range(len(D)):
```

```
  for b in range(len(D[0])):
    D[a][b] = mean(D[a][b])

# We make two empty lists for the Xs and Ys for fitting the slope
xs, ys = [], []

# For background substration we will step through the voltage levels, and when
# we find 0.0, we store the SIGNAL value and remove it from all the SIGNAL
# values. We set this background to zero first, in case no real BG measurement
# was taken.
signal_bg = 0.0
for a in D:
  if a[0] == 0.0:
    signal_bg = a[2]
    print "Using %0.2e as the background value" % signal_bg
if signal_bg == 0.0:
  print "No data at zero drive voltage. No background correction applied!"
for a in D:
  a[2] -= signal_bg
  # Append corrected values to list of points for slope fitting.
  xs.append(a[1])

# Calculating FR-Total and FR-Film. For each wavelength we have a different
# correction factor (given in deg/T/m)
for avg in D:
  FRTotal = -57.296*avg[2]/(800*avg[3])
  if wl=="1550":
    FR = -1*(FRTotal+avg[1]*39.12*1e-7) # Exp fit for BK7 at 1550 nm
    outname = fname_root + "_1550process.csv"
  if wl=="1310":
    FR = -1*(FRTotal+avg[1]*74.0*1e-7) # Lit value for BK7 at 1310 nm
    outname = fname_root + "_1310process.csv"
```

```
    if wl=="980":
      FR = -1*(FRTotal+avg[1]*104.0*1e-7) # Lit value for BK7 at 980 nm
      outname = fname_root + "_980process.csv"
    if wl=="845":
      FR = -1*(FRTotal+avg[1]*146.8*1e-7) # Lit value for BK7 at 845 nm
      outname = fname_root + "_845process.csv"
    if wl=="glass":
      FR = FRTotal # If given "glass" then no correction is applied.
                   # Used for BK7 and TGG.
      outname = fname_root + "_GLASSprocess.csv"

    avg.append( FRTotal )
    avg.append( FR )
    ys.append( FR )

  # Now we write the output file and return the goods
  # to whatever called the function.
  print "Saving file: "+outname
  savetxt(outname, D, delimiter=',')
  return D, xs, ys

# Ask the user what the wavelength and thickness were.
# The thickness is just for Verdet
# constant estimation at the prompt, it does not get
# used for the saved output files.
wl = raw_input('Wavelength or "glass" for substrate correction: ')
thick = float( input('Thickness (mm) for Verdet estimate: ') )

# Call the huge function above, storing the
# processed measures (D) and fitting points
D, xs, ys = read_in_data(fname, wl=wl)
```

```
print "Fitting..."
x = array(xs)[:,newaxis]    # Fix the dimensionality of the array so least-squares
                            # likes it
a = linalg.lstsq(x, ys)     # Find the least-squares solution for Y = A*X
                            # (zero-intercept)
slope = a[0][0]             # Pull the slope from the output of least-squares
V = slope/(1e-7*thick)      # Calculate the Verdet constant in deg/T/m

print "Slope = %0.4e" % slope
print "Verdet constant = %0.3f deg/Tesla/meter" % V
```

Appendix A - Hologram Generation Script (MATLAB)

```
% Binary Intensity Hologram Generation for
% Texas Instruments DMD for MATLAB 2013B,
% based on code by Brittany Lynn, this version by Alex Miles

% Calculates an absorption grating utilizing a Gershberg-Saxton algorithm.
% Analysis completed in 2 dimensions with square symmetry, eg. dx=dy, etc.
% Keep in mind that the assumption is input files labeled 01,02,03 ...  09
% with some possible prefix that is the same for all files.  This way they
% are loaded in order.  Order is

%     1   2
%   3   4   5
%     6   7

clc
clear all
close all

% Change to specify starting path
folder = '/media /Alex_switchstuff/imgs';
% Get the names of all files
dirListing = dir(folder);
pic = 0;
% Loop through the files and open. Note that dir also lists the directories,
% so you have to check for them.
for d = 1:length(dirListing)
if ~dirListing(d).isdir
    pic = pic+1;
```

```
    % Use full path, the folder may not be the active path
    fileName = fullfile(folder,dirListing(d).name);
    a = imread(fileName);
    A_goal_set(:,:,pic) = im2bw(a(:,:,1));
end
end

NX      = 256;
NY      = 256;
thresh  = 0.5; % Binarization threshold
beta    = 0.9;

for ll = 1:pic
    A_goal     = A_goal_set(:,:,ll);
    % Create frequency spectrum of desired intensity pattern
    a_k        = ifft2(A_goal);
    a_k_p      = real(exp(1i*pi*im2bw(angle(a_k),thresh))./2+0.5);
    A_k_p_1    = fft2(a_k_p);
    int        = abs(A_k_p_1).^2;
    norm       = sum(int(:));
    A_k_p      = A_k_p_1/sqrt(norm);
    dA         = abs(A_goal).*(2*exp(1i*angle(A_k_p))-exp(1i*angle(A_goal)))-A_goal;
    A_k_next_1 = (A_k_p + beta*dA).*A_goal;
    inter      = abs(A_k_next_1).^2;
    A_k_next   = A_k_next_1/sqrt(sum(inter(:)));

    for ii=1:100
     a_k      = ifft2(A_k_next);
     a_k_p    = real(exp(1i*pi*im2bw(angle(a_k),thresh))./2+0.5);
     A_k_p_1  = fft2(a_k_p);
     int      = abs(A_k_p_1).^2;
     norm     = sum(int(:));
```

```
     A_k_p    = A_k_p_1/sqrt(norm);
     dA       = abs(A_goal).*(2*exp(1i*angle(A_k_p))-exp(1i*angle(A_k_next)))-A_k_next;
     A_k_next_1 = (A_k_p + beta*dA).*A_goal;
     inter    = abs(A_k_next_1).^2;
     A_k_next = A_k_next_1/sqrt(sum(inter(:)));
    end

    a_k         = ifft2(A_k_next);
    a_k_final   = real(exp(1i*pi*im2bw(angle(a_k),thresh))./2+0.5);
    A_k_final_1 = fftshift(fft2(a_k_final));
    int         = abs(A_k_final_1).^2;
    norm        = sum(int(:));
    A_k_final   = A_k_final_1/sqrt(norm);
    I           = abs(A_k_final).^2;

    ft_store(:,:,ll) = a_k_final;
    I_store(:,:,ll)  = I;
end

%I now have a matrix in which each fourier transform "image" corresponds to
%a different input fiber location.  I need to concatinate them in the
%appropriate order.  This part is only for a 3x3 array - will need to be
%changed for different size output

% Addressing for top row
DMD(1:NX, NX+1+NX/4-NX/2:NX+NX/4+NX/2) = N;%ft_store(:,:,1);
DMD(1:NX, 2*NX+1+NX/4:2*NX+NX/4+NX) = N;%ft_store(:,:,2);

% Adressing for middle row
DMD(NX+1:2*NX, 1:NX) = N;%ft_store(:,:,3);
DMD(NX+1:2*NX, NX+1+NX/2:2*NX+NX/2) = ft_store(:,:,1);
DMD(NX+1:2*NX, 2*NX+1+NX:3*NX+NX) = N;%ft_store(:,:,5);
```

```
% Addressing for bottom row
DMD(2*NX+1:3*NX, NX+1+NX/4-NX/2:NX+NX/4+NX/2) = N;%ft_store(:,:,6);
DMD(2*NX+1:3*NX, 2*NX+1+NX/4:2*NX+NX/4+NX) = N;%ft_store(:,:,7);

imshow(DMD)
```

Appendix C - Merit Function Script (Macleod Essential)

```
' Scripted Merit Function for Balancing Current-Matched
' Photovoltaic Cells Over a Variety of Angles
'
' This function requires DesignSet.bas, DesignConstants.bas
'
' Alex Miles - Originated 9/30/2014
'            - Last edit  4/20/2015
'
Dim YAxis As Object
Dim Sun As Object
Dim wl As Double
Dim w_start As Double
Dim w_end As Double
Dim w_step As Double
Dim N As Double
Dim index As Long

Function delta(Angle As Double) As Double

        Dim XAxis As Object
        Dim YAxis As Object
        Dim wl As Double
        Dim w_start As Double
        Dim w_end As Double
        Dim w_step As Double
        Dim N As Double
        Dim index As Long
        Dim bucket_one As Double
```

```
Dim bucket_two As Double
Dim hc As Double ' For conversion to photon-count
Dim want_T As Double
Dim T_count As Double
Dim want_R As Double
Dim R_count As Double
Dim cutoff_one As Double 'Cutoff wavelegnth for top junction
Dim cutoff_two As Double  'Cutoff wavelegnth for top junction

hc = 1.986446E-16 ' joule-nanometers
bucket_one = 0
bucket_two = 0
want_T = 0
T_count = 0
want_T = 0
T_count = 0

cutoff_one = 659.5 'nanometer, from 1.88 eV
cutoff_two = 850.0 ' originally 850.0 nanometer from 1.47 eV

Set XAxis = ThisDesign.XAxisParameters
Set YAxis = ThisDesign.YAxisParameters

 W_start = 300
W_end = 2500
W_step = 1
N = (W_end - W_start)/(W_step)

XAxis.CalculationIncidentAngle = Angle
Set YAxis = ThisDesign.YAxisParameters
Set DataSet = ThisDesign.CalculateTable(XAxis, YAxis)
```

```
Dim power(2200) As Double
Dim photons(2200) As Double
Dim wavelength(2200) As Double

For wl = W_start To W_end Step W_step
                index = (wl - W_start)/W_step
                power(index) = Sun.GetValue(wl)
                wavelength(index) = wl
                photons(index) = Sun.GetValue(wl)*wl/(hc)_
                                 *DataSet.InterpolateYMean(wl)

                 If ( (wl < 510) Or (wl > 740 ) ) Then
                        want_T = want_T + DataSet.InterpolateYMean(wl)
                        T_count = T_count + 1
                 Else
                        want_R = want_R + DataSet.InterpolateYMean(wl)
                        R_count= R_count + 1
                 End If

                If (wl > 460 And wl < cutoff_one) Then
                        bucket_one = bucket_one + photons(index)
                ElseIf wl < cutoff_two And wl > cutoff_one Then
                        bucket_two = bucket_two + photons(index)
                End If
Next wl

Dim bigger As Double
bigger = bucket_one

If bucket_one > bucket_two Then
        bigger = bucket_one
Else
```

```
                bigger = bucket_two
        End If

        delta = 240*want_T/T_count +_
                 60*Abs(bucket_one-bucket_two)/bigger +_
                 25*(1-want_R/R_count)
End Function

Sub Initialize()
        Set Sun = CreateObject("EMacleod.Reference")
        Sun.LoadReference "AM1p5.ref"  ' Contains the AM1.5g solar spectrum
        cell_one = 659.5
        cell_two = 867.0
End Sub

Function MeritFunction() As Double
  MeritFunction = (0.176*delta(11.25) + 0.284*delta(15) + 0.365*delta(18.75)_
                + 0.429*delta(22.5)  + 0.505*delta(26.25) + 0.565*delta(30.0)_
                + 0.647*delta(33.75) + 0.723*delta(37.50) + 0.805*delta(41.25)_
                + 0.899*delta(45) + 1.00*delta(48.75) + 0.831*delta(52.5)_
                + 0.442*delta(56.25) + 0.272*delta(60) + 0.140*delta(63.75) )^2
End Function
```

REFERENCES

[1] FE Adkins. Raccoon mountain pumped-storage plant-ten years operating experience. *Energy Conversion, IEEE Transactions on*, 1(3):361–368, 1987.

[2] Govind P Agrawal. *Lightwave Technology: Components and Devices*, volume 1. John Wiley & Sons, 2004.

[3] M Alagiri, C Muthamizhchelvan, and S Ponnusamy. Structural and magnetic properties of iron, cobalt and nickel nanoparticles. *Synthetic Metals*, 161(15):1776–1780, 2011.

[4] Stephen B Alexander. Wavelength division multiplexed optical communication systems employing uniform gain optical amplifiers, December 9 1997. US Patent 5,696,615.

[5] IA Apolonskaya, AV Tyurnina, PG Kopylov, and AN Obraztsov. Thermal oxidation of detonation nanodiamond. *Moscow University Physics Bulletin*, 64(4):433–436, 2009.

[6] European Photovoltaic Industry Association et al. Global market outlook for photovoltaics 2014–2018.[online] available: http://www. epia. org/filead min/user_upload. *Publications/44_epia_gmo_report_ver_ 17_mr. pdf*, 2014.

[7] Norman P Barnes and Larry B Petway. Variation of the verdet constant with temperature of terbium gallium garnet. *JOSA B*, 9(10):1912–1915, 1992.

[8] Richard E Bird and Roland L Hulstrom. Simplified clear sky model for direct and diffuse insolation on horizontal surfaces. Technical report, Solar Energy Research Inst., Golden, CO (USA), 1981.

[9] Myron K Brakke. Density-gradient centrifugation. *Methods in Virology*, 2:93–118, 1967.

[10] Joy Y Cheng, CA Ross, EL Thomas, Henry I Smith, and GJ Vancso. Fabrication of nanostructures with long-range order using block copolymer lithography. *Applied Physics Letters*, 81(19):3657–3659, 2002.

[11] Cisco. Cisco Global Cloud Index: Forecast and Methodology, 2012-2017. Technical report, Cisco, 07 2013.

[12] WA Crossland, IG Manolis, MM Redmond, KL Tan, TD Wilkinson, MJ Holmes, TR Parker, HH Chu, J Croucher, VA Handerek, et al. Holographic optical switching: the" roses" demonstrator. *Lightwave Technology, Journal of*, 18(12):1845–1854, 2000.

[13] Louis-anne De Montmorillon, Denis Molin, Marianne Bigot-Astruc, and Pierre Sillard. Chromatic dispersion compensating fiber, April 2008. US Patent 7,356,234.

[14] MN Deeter, GW Day, and AH Rose. Crc handbook of laser science and technology, supplement 2: Optical materials. *CRC, Boca Raton*, 1995.

[15] L. DeSandre, D. Y. Song, H. A. MacLeod, M. R. Jacobson, and D. E. Osborn. Thin-film multilayer filter designs for hybrid solar energy conversion systems. *Proceedings of the SPIE - The International Society for Optical Engineering*, 562:155–9, 1985.

[16] Michael R Douglass. Lifetime estimates and unique failure mechanisms of the digital micromirror device (dmd). In *Reliability Physics Symposium Proceedings, 1998. 36th Annual. 1998 IEEE International*, pages 9–16. IEEE, 1998.

[17] J. C. C. Fan and F. J. Bachner. Transparent heat mirrors for solar-energy applications. *Applied Optics*, 15(4):1012–1017, 1976.

[18] M Faraday. Faraday's diary. volume iv, nov. 12, 1839-june 26, 1847, 1933.

[19] Nathan Farrington, George Porter, Sivasankar Radhakrishnan, Hamid Hajabdolali Bazzaz, Vikram Subramanya, Yeshaiahu Fainman, George Papen, and Amin Vahdat. Helios: a hybrid electrical/optical switch architecture for modular data centers. *ACM SIGCOMM Computer Communication Review*, 41(4):339–350, 2011.

[20] Nathan Farrington, George Porter, Pang-Chen Sun, Alex Forencich, Joseph Ford, Yeshaiahu Fainman, George Papen, and Amin Vahdat. A demonstration of ultra-low-latency data center optical circuit switching. *ACM SIGCOMM Computer Communication Review*, 42(4):95–96, 2012.

[21] JR Fienup. Iterative method applied to image reconstruction and to computer-generated holograms. *Optical Engineering*, 19(3):193297–193297, 1980.

[22] Charles W Forsberg, Per F Peterson, and Haihua Zhao. High-temperature liquid-fluoride-salt closed-brayton-cycle solar power towers. *Journal of Solar Energy Engineering*, 129(2):141–146, 2007.

[23] Bruno Fracasso, JL de Bougrenet de La Tocnaye, M Razzak, and C Uche. Design and performance of a versatile holographic liquid-crystal wavelength-selective optical switch. *Lightwave Technology, Journal of*, 21(10):2405–2411, 2003.

[24] Palash Gangopadhyay, Ramakrishna Voorakaranam, Alejandra Lopez-Santiago, Stijn Foerier, Jayan Thomas, Robert A Norwood, Andre Persoons, and Nasser Peyghambarian. Faraday rotation measurements on thin films of regioregular alkyl-substituted polythiophene derivatives. *The Journal of Physical Chemistry C*, 112(21):8032–8037, 2008.

[25] Andreas Gehner. Mems adaptive optics development at ipms. *Fraunhofer IPMS retrieved from retrieved April*, 2014.

[26] Joseph W Goodman. *Introduction to Fourier Optics*. Roberts and Company Publishers, 2005.

[27] Martin A Green, Keith Emery, Yoshihiro Hishikawa, Wilhelm Warta, and Ewan D Dunlop. Solar cell efficiency tables (version 45). *Progress in Photovoltaics: Research and Applications*, 23(1):1–9, 2015.

[28] Jeff Hecht. *Understanding Fiber Optics*. Jeff Hecht, 2015.

[29] Houjin Huang, Liming Dai, David H Wang, Loon-Seng Tan, and Eiji Osawa. Large-scale self-assembly of dispersed nanodiamonds. *Journal of Materials Chemistry*, 18(12):1347–1352, 2008.

[30] K Iakoubovskii, K Mitsuishi, and K Furuya. High-resolution electron microscopy of detonation nanodiamond. *Nanotechnology*, 19(15):155705, 2008.

[31] A. G. Imenes, D. Buie, and D. McKenzie. The design of broadband, wide-angle interference filters for solar concentrating systems. *Solar Energy Materials and Solar Cells*, 90(11):1579–1606, 2006.

[32] A. G. Imenes, D. Buie, D. R. Mills, P. Schramek, and S. G. Bosi. A new strategy for improved spectral performance in solar power plants. *Solar Energy*, 80(10):1263–1269, 2006.

[33] A. G. Imenes and D. R. Mills. Spectral beam splitting technology for increased conversion efficiency in solar concentrating systems: a review. *Solar Energy Materials and Solar Cells*, 84(1-4):19–69, 2004.

[34] Texas Instruments. DLP Discovery 4100 Digital Controller Data Sheet. Technical report, Texas Instruments, 2012.

[35] ISO. Information techonology - open systems interconnection - basic reference model. ISO 7498-1, International Standards Organization, June 1996.

[36] Herwig Kogelnik. Coupled wave theory for thick hologram gratings. *Bell System Technical Journal*, 48(9):2909–2947, 1969.

[37] Andrew M Kowalevicz Jr and Frank Bucholtz. Beam divergence from an smf-28 optical fiber. Technical report, DTIC Document, 2006.

[38] Anke Krueger. The structure and reactivity of nanoscale diamond. *Journal of Materials Chemistry*, 18(13):1485–1492, 2008.

[39] Ohad Levy and David Stroud. Maxwell garnett theory for mixtures of anisotropic inclusions: Application to conducting polymers. *Physical Review B*, 56(13):8035, 1997.

[40] Yanming Liu and Mark A Newhouse. Large effective area waveguide fiber, November 10 1998. US Patent 5,835,655.

[41] Brittany Lynn, Pierre-Alexandre Blanche, Alan Miles, John Wissinger, Daniel Carothers, Lloyd LaComb, Robert Norwood, Nasser Peyghambarian, et al. Design and preliminary implementation of an n n diffractive all-optical fiber optic switch. *Lightwave Technology, Journal of*, 31(24):4016–4021, 2013.

[42] H Angus Macleod. *Thin-film Optical Filters*. CRC Press, 2010.

[43] Eric Martinot et al. *Renewables 2014: Global status report*. Worldwatch Institute Washington, DC, 2014.

[44] Eric Marx. How solar-heavy europe avoided a blackout during total eclipse, March 2015. ScientificAmerican.com [Online; posted 24-March-2015].

[45] Robert J Mears, L Reekie, IM Jauncey, and David N Payne. Low-noise erbium-doped fibre amplifier operating at 1.54 μm. *Electronics Letters*, 23(19):1026–1028, 1987.

[46] Stewart Miller. *Optical Fiber Telecommunications*. Elsevier, 2012.

[47] Nafiseh Moghimi and KT Leung. Fept alloy nanoparticles for biosensing: enhancement of vitamin c sensor performance and selectivity by nanoalloying. *Analytical Chemistry*, 85(12):5974–5980, 2013.

[48] Ahmad Mojiri, Cameron Stanley, and Gary Rosengarten. Spectrally splitting hybrid photovoltaic/thermal receiver design for a linear concentrator. *Proceedings of the 2nd International Conference on Solar Heating and Cooling for Buildings and Industry (Shc 2013)*, 48:618–627, 2014.

[49] CSR Murthy and M Gurusamy. Wdm optical networks, concepts, design and algorithms. *Pretince Hall PTR*, 2002.

[50] Renewable Energy Policy Network. Renewables 2014 global status report. *Renewable Energy Policy Project.(1999). Renewable Energy Policy Outside the US. Retrieved from http://www. uea. ac. uk/˜ e680/energy/energy_links/renewables_Obligation/Nffo_review. htm*, 2014.

[51] Rachel K O'Reilly, Craig J Hawker, and Karen L Wooley. Cross-linked block copolymer micelles: functional nanostructures of great potential and versatility. *Chemical Society Reviews*, 35(11):1068–1083, 2006.

[52] D. E. Osborn, M. A. C. Chendo, M. A. Hamdy, F. Luttmann, M. R. Jacobson, H. A. Macleod, and R. Swenson. Spectral selectivity applied to hybrid concentration systems. *Solar Energy Materials*, 14(3-5):299–325, 1986.

[53] Günter Reiss and Andreas Hütten. Magnetic nanoparticles: applications beyond data storage. *Nature Materials*, 4(10):725–726, 2005.

[54] Olivier Ripoll, Ville Kettunen, and Hans Peter Herzig. Review of iterative fourier-transform algorithms for beam shaping applications. *Optical Engineering*, 43(11):2549–2556, 2004.

[55] John H Seinfeld and Spyros N Pandis. *Atmospheric chemistry and Physics: From Air Pollution to Climate Change*. John Wiley & Sons, 2012.

[56] Gary D Shaffer. An archaeomagnetic study of a wattle and daub building collapse. *Journal of Field Archaeology*, 20(1):59–75, 1993.

[57] Element Six. Enable the impossible. *Element Six retrieved from http://www.e6.com/ retrieved October 2015*, 2014.

[58] Xiaoming Sun, Scott M Tabakman, Won-Seok Seo, Li Zhang, Guangyu Zhang, Sarah Sherlock, Lu Bai, and Hongjie Dai. Separation of nanoparticles in a density gradient: Feco@ c and gold nanocrystals. *Angewandte Chemie International Edition*, 48(5):939–942, 2009.

[59] Calient Technologies. S320 photonic switch data sheet. Technical report, Calient Technologies, inc., 2013.

[60] AV Tyurnina, IA Apolonskaya, II Kulakova, PG Kopylov, and AN Obraztsov. Thermal purification of detonation diamond. *Journal of Surface Investigation. X-ray, Synchrotron and Neutron Techniques*, 4(3):458–463, 2010.

[61] VK Valev, J Wouters, and Thierry Verbiest. Precise measurements of faraday rotation using ac magnetic fields. *American Journal of Physics*, 76(7):626–629, 2008.

[62] Vitruvius Vitruvius. *Ten Books on Architecture*. eKitap Projesi, 2015.

[63] A. S. Vlasov, V. P. Khvostikov, L. B. Karlina, S. V. Sorokina, N. S. Potapovich, M. Z. Shvarts, N. Kh Timoshina, V. M. Lantratov, S. A. Mintairov, N. A. Kalyuzhnyi, E. P. Marukhina, and V. M. Andreev. Spectral-splitting concentrator photovoltaic modules based on algaas/gaas/gasb and gainp/ingaas(p) solar cells. *Technical Physics*, 58(7):1034–1038, 2013.

[64] RE Wagner and WJ Tomlinson. Coupling efficiency of optics in single-mode fiber components. *Applied Optics*, 21(15):2671–2688, 1982.

[65] RR Willey. Field guide to optical thin films. Technical report, SPIE, 2006.

[66] Peter Würfel and Uli Würfel. *Physics of Solar Cells: From Basic Principles to Advanced Concepts*. John Wiley & Sons, 2009.

[67] Frank Wyrowski. Diffractive optical elements: iterative calculation of quantized, blazed phase structures. *JOSA A*, 7(6):961–969, 1990.

[68] Susanne Zwick, Tobias Haist, Michael Warber, and Wolfgang Osten. Dynamic holography using pixelated light modulators. *Applied optics*, 49(25):F47–F58, 2010.